Quaternary Science Reviews 372 (2026) 109715

Contents lists available at ScienceDirect

Quaternary Science Reviews

journal homepage: www.elsevier.com/locate/quascirev

Post-LGM sedimentation history and deglaciation processes in the southern Gulf of St. Lawrence, Canada

I. Schulten [a,*], V. Maselli [a,b], E.L. King [c], M. Schmidt [d], C. Hensen [d], T. Müller [d,e], A. Asioli [f], A. Micallef [g], C. Berndt [d], C.J. Brown [h], F. Córdoba-Ramírez [a], J. Elger [d,i], S. Hölz [d], A. Kotliarov [j], B. Kurylyk [k], S. Yu [k], M.R. Nedimović [a]

[a] Department of Earth and Environmental Sciences, Dalhousie University, Halifax, Nova Scotia, Canada
[b] Department of Chemical and Geological Sciences, University of Modena and Reggio Emilia, Modena, Italy
[c] Natural Resources Canada (NRCan), Geological Survey of Canada Atlantic, Dartmouth, Nova Scotia, Canada
[d] GEOMAR Helmholtz Centre for Ocean Research Kiel, RD2/Marine Geosystems, RD4/Marine Geodynamic, Kiel, Germany
[e] Department Hydrogeology, Helmholtz Centre for Environmental Research GmbH - UFZ, Leipzig, Germany
[f] Institute of Marine Sciences (CNR-ISMAR), Bologna, Italy
[g] Monterey Bay Aquarium Research Institute (MBARI), Moss Landing, CA, USA
[h] Department of Oceanography, Dalhousie University, Halifax, Nova Scotia, Canada
[i] Department of Geoscience, Aarhus University, Aarhus C, Denmark
[j] Fisheries and Marine Institute, Memorial University of Newfoundland, Newfoundland and Labrador, Canada
[k] Department of Civil and Resource Engineering and Centre for Water Resources Studies, Dalhousie University, Halifax, Nova Scotia, Canada

ARTICLE INFO

Handling editor: Bethan Davies

ABSTRACT

During the last glacial period, continents and surrounding shelves in high latitude regions of the Northern Hemisphere were covered by ice sheets. Their retreat after the Last Glacial Maximum resulted in isostatic adjustments of the previously glaciated landmass and post-glacial changes in relative sea level during the late Pleistocene and Holocene. Many questions, however, remain about the timing and impact of the ice retreat and of short-lived climatic events on continental shelf environments. This study aims to reconstruct the sedimentation and deglaciation processes on the continental shelf of the southern Gulf of St. Lawrence (Canada) over the past 14 ka by investigating changes in the sedimentation patterns and paleo-environments. Using information from sub-bottom profiles, sediment cores, and multibeam bathymetry, this study finds that most of the continental shelf was flooded 13.6 ka ago, as evidenced by the presence of Bølling-Allerød marine sediments at a water depth of ~50 m and ~15 km off the modern coastline, which also suggests an earlier retreat of the Laurentide Ice Sheet than suggested by previous studies. We estimate sedimentation rates for the Bølling-Allerød of ~0.4 cm a^{-1}, which increased up to 1 cm a^{-1} during the Younger Dryas cooling event, likely associated with increased storm-wave activity and sea ice development caused by deteriorating climatic conditions. The presence of an erosional truncation atop Younger Dryas sediments indicates a late Pleistocene-early Holocene relative sea level fall and associated lowstand. Based on our new data, we established a geological model that highlights sedimentation processes since the Last Glacial Maximum and demonstrate the potential impact of short-lived climatic events on the former ice margin during deglaciation.

1. Introduction

The Pleistocene glaciations significantly shaped the modern landscape of the Northern Hemisphere. During the last cold period, which culminated in the Last Glacial Maximum (LGM) between 26 and 18 ka BP (Clark et al., 2009), the high latitude regions of North America and their adjacent continental shelves were covered by the Laurentide Ice Sheet (LIS) (e.g., Dyke et al., 2003; Shaw, 2005; Shaw et al., 2006; Stokes, 2017; Dalton et al., 2020). The glaciations left behind specific depositional and erosional features, both onshore and offshore, which provide essential information about the ice dynamics (Shaw et al., 2006, 2009; Winsborrow et al., 2010; Evans and Evans, 2022). Over the past

* Corresponding author.
E-mail address: irena.schulten@dal.ca (I. Schulten).

https://doi.org/10.1016/j.quascirev.2025.109715
Received 26 March 2025; Received in revised form 13 November 2025; Accepted 17 November 2025
Available online 25 November 2025

few decades, several studies aimed to quantify how the LIS advanced and retreated, especially following the LGM (e.g., Stea et al., 1998; Dyke et al., 2003; Stea, 2011; Stokes, 2017; Dalton et al., 2020). The impact of short-lived climatic oscillations on the ice sheet dynamics, such as the Younger Dryas cooling event (12.9–11.6 ka BP), are, however, still debated (e.g., Loring and Nota, 1973; Fairbanks, 1989; Stea and Mott, 1998, 2005; Stea et al., 1998; Dalton et al., 2024). Ice retreat at the end of the last glaciation caused isostatic adjustments in many high latitude regions. Over time, a collapse of the forebulge margin and hydro-isostatic loading along coastlines instigated subsidence of the former glaciated margins such as observed in parts of eastern Canada (Forbes et al., 2014), and many regions still experience a rise in relative sea level to this day (RSL; IPCC, 2023). A precise quantification of the extent and retreat history of the former ice sheets, particularly along their margins (i.e., the modern continental shelves) is therefore key to improving our current understanding about ice sheet dynamics and associated RSL changes.

In our study area, the southern Gulf of St. Lawrence offshore of Prince Edward Island (PEI) in Eastern Canada (Fig. 1a), a retreat of the LIS following the LGM is presumed to have resulted in an early RSL drop due to isostatic uplift (e.g., Forbes et al., 2004, 2014; Shaw et al., 2002, 2006, 2009; Vacchi et al., 2018). Ice sheet retreat was likely interrupted during the Younger Dryas, when a short-lived ice re-advance or ice buildup may have occurred (Stea et al., 1998; Shaw, 2005; Shaw et al., 2006, 2009; Vacchi et al., 2018). Its exact extent and influence on sedimentation and RSL for this region is, however, highly debated (e.g., Loring and Nota, 1973; Stea and Mott, 1989, 1998). Following the Younger Dryas, the margin likely experienced a rise in RSL starting at ~9 ka BP in response to isostatic subsidence related to movement of the forebulge margin (Forbes et al., 2004, 2014). This subsidence and RSL rise persists until today at a rate of 3.2 mm a^{-1}, which is much faster than the global average (Carr, 1969; Forbes et al., 2004; Barlow and Reichard, 2010). The high rate of RSL rise causes significant problems to coastal communities situated in the region as it increases their vulnerability to coastal flooding, erosion, and saltwater intrusion (SWI) into onshore aquifers (Forbes et al., 2014; Stanic et al., 2024).

Open questions remain regarding the sedimentation history in the southern Gulf of St. Lawrence since the LGM and the influence and extent of the Younger Dryas. This information is important to improve RSL reconstructions and predictions for Atlantic Canada. In this study, we aim to identify changes in sedimentation patterns and paleo-environments in the southern Gulf of St. Lawrence following the LGM to reconstruct the local deglaciation history and infer associated changes in RSL using newly acquired multibeam bathymetry, sub-bottom seismic profiles and sediment cores (Fig. 1b and c, S1, S2). The new findings improve environmental reconstructions for the region and provide key information about paleo-ice limits and buried drainage systems, offering geological constraints that advance understanding of how onshore and offshore aquifers are linked (cf. Edmunds et al., 2001; Yu et al., 2025).

2. Regional geology

The southern Gulf of St. Lawrence is a semi-enclosed basin of ~61,500 km^2 located on the Eastern Canadian continental shelf. It is bordered to the west by New Brunswick, to the south by PEI and Nova Scotia, respectively, to the east by Cape Breton Island of Nova Scotia, and to the north by the Laurentian Channel (Fig. 1a). The shelf generally consists of a plateau with rugged or uneven terrain, networks of shallow channels and up to 200 m deep topographic depressions such as the Cape Breton Trough (CBT) located in its eastern portion (Fig. 1a and b) (e.g., Loring and Nota, 1973; Pinet and Brake, 2024). Most of the channels are NE-oriented towards the Laurentian Channel, while 70–80 m deep EW-trending channel systems are present between PEI and the Magdalen Islands that lead towards the CBT (Fig. 1a and b).

The region is part of the Maritime Basin, which is filled with Devonian to Permian terrigenous fluvio-deltaic and shallow-marine sandstones and shales that were primarily deposited under arid and semi-arid conditions (Carr, 1969; Van de Poll, 1989; Symons, 1990; Gibling et al., 2019). These strata are widely known as the PEI grey- and red-beds due to their distinctive color and exposure throughout the island (Carr,

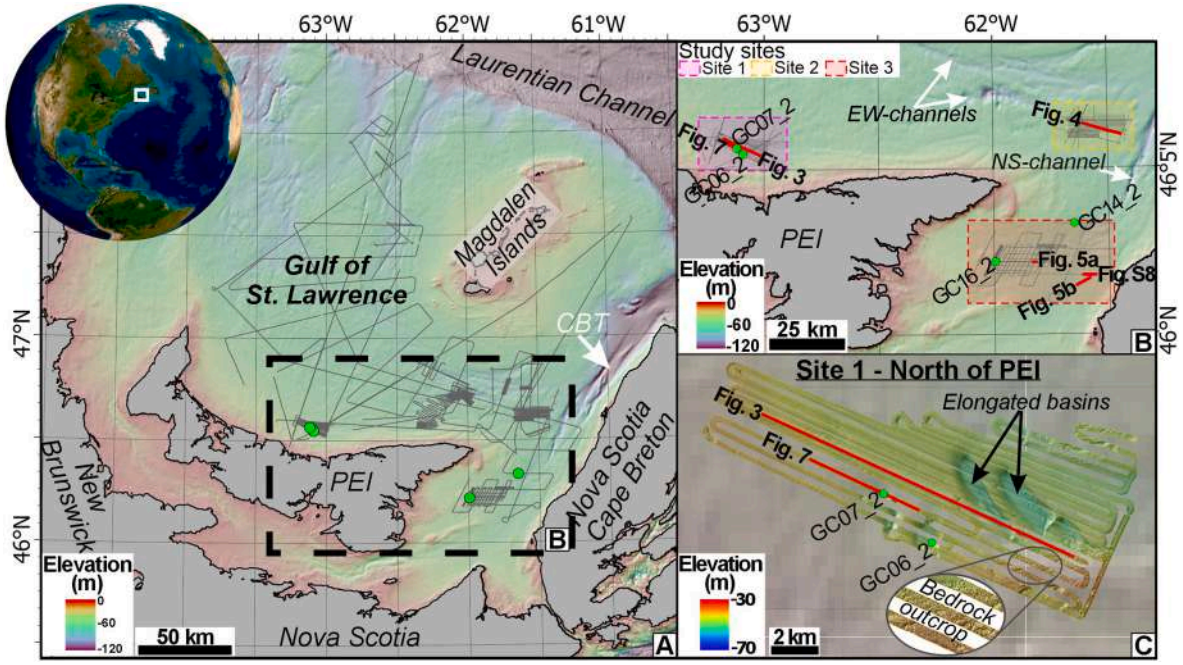

Fig. 1. A) Overview of the study area in the southern Gulf of St. Lawrence; B) zoom to study sites that are located north (Site 1, pink box), northeast (Site 2, yellow box) and east (Site 3, red box) of PEI; and C) multibeam bathymetry map of Site 1. Grey lines are the sub-bottom profiles acquired during MSM103 with the ones used in this study shown in B), while the red lines are the profiles presented in the figures. Green dots show the location of sediment cores selected for this study. Morphologically significant sites and special characteristics are highlighted. CBT stands for Cape Breton Trough. The maps were generated using ArcGIS Pro® and background bathymetric data from GEBCO. (For interpretation of the references to color in this figure legend, the reader is referred to the Web version of this article.)

1969; Van de Poll, 1989). The Paleozoic rocks are directly covered by Quaternary sediments (Carr, 1969; Loring and Nota, 1973; Jiang and Somers, 2009).

The Pleistocene glaciations, and particularly the last one, significantly altered the preglacial landscape (Loring and Nota, 1973). At the climax of the LGM, the LIS extended across North America to the edge of the Eastern Canadian continental shelf (e.g., Stea and Mott, 1989; Stea et al., 1998; Shaw et al., 2006; Stea, 2011). Following the LGM, an increase in global temperatures led to a thinning of the ice mass across PEI and Nova Scotia, and resulted in major calving episodes with massive ice streams through the Laurentian Channel (Shaw et al., 2006, 2009; Stea, 2011). The ice retreated rapidly from the Gulf of St. Lawrence and by 13 ka BP most of the ice mass was onshore in the form of localized ice centers (Stea and Mott, 1989; Shaw et al., 2006, 2009; Stea, 2011), with one located on PEI (Loring and Nota, 1973; Stea et al., 1998; Vacchi et al., 2018). The Younger Dryas cooling event likely resulted in a re-advance of the isolated marine and terrestrial ice remnants and potential formation of new ice caps (Stea and Mott, 1989; Stea et al., 1996, 1998; Shaw et al., 2006; Stea, 2011; Vacchi et al., 2018). Global warming after the Younger Dryas led to a complete removal of the ice mass from the Gulf of St. Lawrence by 10 ka BP (Vacchi et al., 2018).

Each ice retreat and re-advance was likely accompanied by marine transgressions and regressions, driven by a combination of eustatic changes and local tectonic movements (Fairbanks, 1989; Shaw et al., 2002; Person et al., 2003; Forbes et al., 2014). Previous studies suggested that the Gulf of St. Lawrence was rapidly flooded between 16 and 12 ka BP (Loring and Nota, 1973; Forbes et al., 2004, 2014), but isostatic rebound caused an uplift of the entire region that led to a RSL lowstand between 10 and 9 ka BP down to approximately −40 m and subaerial exposure of parts of the continental shelf (Shaw et al., 2002; Shaw, 2005; Forbes et al., 2014; Vacchi et al., 2018). RSL rose following this lowstand, as a collapse of the forebulge margin and hydro-isostatic loading caused tectonic subsidence over the past 9 to 10 ka (Pirazzoli, 1991; Shaw et al., 2002; Forbes et al., 2004, 2014). From 6 ka BP, this subsidence was less pronounced but continues to this day (Forbes et al., 2004, 2014).

3. Methods

This study focuses on three study sites with the highest data density, which are located north, northeast and east of PEI, and termed Site 1, 2 and 3 respectively (Fig. 1b). All geophysical data and sediment cores were collected during the 60-day-long research expedition MSM103 in 2021 onboard of the R/V Maria S. Merian (Hölz, 2022).

3.1. Hydroacoustic data sets

3.1.1. Multibeam echosounder data

Multibeam echosounder data were acquired using the Kongsberg Simrad EM712 system. This system operates at a nominal frequency of 40–100 kHz and allows data acquisition between 5 and 3600 m water depth (mwd) (Kongsberg, 2022). Bathymetric data were processed using the open access software MB-System (version 5.8.1), gridded at 2 m resolution, and used for geomorphological characterization.

3.1.2. Sub-bottom profiles

Sub-bottom profiles were acquired using the Atlas Parasound P70 acquisition system. This parametric echo-sounder operates at 4 kHz. In the Gulf of St. Lawrence, the imaging depth is 10–45 m depending on the sediment thickness, composition and presence of gas-charged sediments. The data have a vertical resolution of 0.15 m calculated considering a sound velocity of 1500 m s^{-1} and a minimum horizontal resolution of 3.5–14 m between 50 and 200 mwd (Spieß, 1993; Teledyne Marine, 2017). Further specifications on data acquisition during MSM103 are provided in the cruise report (Hölz, 2022). The software KingdomSuite™ was used to analyze the sub-bottom profiles and generate surface maps of key reflection horizons needed for paleo-morphological reconstructions and to understand the role of sediment transport, deposition, and erosion in the study sites. For both seismic profiles and maps the depth is in two-way travel time (TWTT, ms) from sea level. We converted the travel time (s) to depth (m) using a sound-velocity of 1500 m s^{-1}, as can be expected for water saturated unconsolidated sediments.

3.2. Sediment analysis

Eight gravity cores, 0.66–4.62 m in length, were collected north, northeast and east of PEI and were split, lithologically described, and sampled onboard (Hölz, 2022). Four sediment cores recovered from Sites 1 and 3 and named GC06_2, GC07_2, GC14_2 and GC16_2 (Fig. 1b) were further sampled for grain size analysis, radiocarbon dating and foraminifera extraction needed for environmental reconstructions. No sediment core was available directly from Site 2 (Fig. 1b).

3.2.1. Grain size

A total of 148 sediment samples were extracted every 10 cm from the four sediment cores for grain size analysis (GC06_2, GC07_2, GC14_2, GC16_2). All samples were treated with 50 ml of hydrogen peroxide (H_2O_2) to remove organic components and dispersed with a Hydro EV unit before being analyzed with a Mastersizer Malvern 3000 at the University of Modena and Reggio Emilia.

3.2.2. Age control

Twenty samples consisting of whole shells, mixtures of benthic and planktonic foraminifera, as well as wood and plant remains were extracted for AMS Radiocarbon dating at the Póznan Radiocarbon Laboratory. The open access software OxCal version 4.4 was used to calibrate the measured ^{14}C values (Ramsey, 2009). A regional modern correction factor (ΔR -83 ± 50) was applied for the Gulf of St. Lawrence (McNeely et al., 2006). Given the differences in the dating material, two separate calibration curves – terrestrial (IntCal20, Reimer et al., 2020) and marine (marine20, Heaton et al., 2020) – were used for the calibration. The dates are reported in cal ka BP with a 2-sigma range to constrain the age model and are correlated to sub-bottom profiles.

3.2.3. Foraminifera analysis and paleo-environmental reconstruction

Fifteen, 1-cm-thick sediment samples were collected from the cores GC06_2, GC07_2, GC14_2, GC16_2 for foraminifera analysis. The samples were dried at 50 °C and washed through a 63 μm mesh sieve. The relatively high amount of fine sand in the washed fraction strongly diluted the foraminifera specimens, and therefore the washed samples were further sieved with 106 μm and 125 μm meshes. The fraction >125 μm was examined for foraminifera analysis, and the fraction between 106 and 125 μm was checked for the presence of taxa with elongated shape (e.g., *Fursenkoina*) or small adult specimens. A semiquantitative analysis at species level was carried out. The taxonomy is based on Brady (1884), Vilks (1969, 1989), Hansen and Lykke-Andersen (1976), Scott et al. (1977, 1980), Schafer and Cole (1982), Vilks et al. (1982), Schröder-Adams et al. (1990), Thomas et al. (1990), Scott and Vilks (1991), Jennings and Helgadottir (1994), Cage et al. (2021) and the nomenclature updated according to Hayward et al. (2025) (see Table S1 for details). The main taxa are illustrated in Supplementary Material Plate I and II.

4. Results

4.1. Geomorphology of the study sites

Site 1 is located ~14 km north of PEI in 40–50 mwd (Fig. 1b and c). The seafloor topography is generally smooth and almost flat within an otherwise rugged seafloor terrain, which can be observed in the northern and southern portions of this site (Fig. 1c). NW- to SE-oriented

depressions with up to 7 m deep relief are evident across the central to eastern portions of Site 1 (Fig. 1c). Site 2 is located ~30 km northeast of PEI at 60 to 70 mwd, and 10 km south of the EW-trending channel systems present between PEI and the Magdalen Islands (Fig. 1a and b, S1). The seafloor at this site shows an overall smooth and flat topography, except for some wavy or undulating bedforms located in the northwestern portion (Fig. S1). Site 3 is located ~25 km to the east of PEI at 45 to 60 mwd (Fig. 1b), and the seafloor comprises a mix of rugged and smooth topography (Fig. 1b–S2). A NE-oriented channel system is noticeable to the east of Site 3 in proximity to Cape Breton, and leads towards Site 2 and the CBT (Fig. 1a and b).

4.2. Seismic stratigraphy

Five major reflection horizons (R1 to R5) plus the seafloor (Sf), and six acoustic units (U0 to U5) were identified based on their distinct reflection characteristics and mapped along the three study sites (Fig. 2, Table 1). The reflection horizons generally confine the units on either the top or bottom, except for R6, which is a characteristic internal reflection within U5 (Fig. 2, Table 1).

4.2.1. Unit U0

In the three study sites, buried depressions are located within U0, which is characterized by no sub-bottom reflections or high amplitude incoherent, often dipping sub-bottom reflections (Fig. 2). Limitations in the acoustic penetration prevent the imaging of the base of U0.

4.2.2. Horizon R1 and unit U1

R1 is the lowermost mappable horizon imaged in sub-bottom profiles crossing the buried depressions (<40 ms or <30 m deep, e.g., Sites 1 and 3) (Fig. 2). It is a high amplitude reflection that is often incoherent and locally not visible due to the limited acoustic penetration depth of the sub-bottom profiles (e.g., depressions at Site 2; >60 ms or >45 m deep) (Figs. 3 and 4). Unit U1 on top of horizon R1 varies in thickness between 2.5 and 12 ms or ~2 and 9 m (Fig. 3, Table 1). This unit is generally transparent with no apparent sub-bottom reflections (Figs. 2–4; Table 1). At times, single incoherent, high amplitude reflections are noticeable within U1, especially in sub-bottom profiles from Site 2 (Fig. 4).

4.2.3. Horizon R2 and unit U2

R2 is present within all sub-bottom profiles and is the lower reflection of a high-amplitude, coherent, hummocky double reflection on top of U1 (Fig. 2). This horizon is mostly conformable to R1, except where U1 shows a larger increase in thickness (Figs. 2, 4 and 5a). Both horizons R1 and R2 form topographic heights within the sub-bottom depressions (Figs. 3 and 5a & b). Unit U2 is found on top of R2 and varies in thickness between 1.5 and 13 ms or ~1 and 10 m (Figs. 2, 4 and 5a; Table 1). It shows coherent, generally low amplitude, stratified reflections that are conformable to horizon R2 (Figs. 2–4, 5a). U2 is primarily present within deeper depressions and can be locally absent, especially at Sites 1 and 3 (Figs. 3 and 5a & b). At Site 2, a change in amplitude of U2 is noticeable with higher reflection amplitudes present along the sides of deeper depressions (Fig. 4; Table 1). These higher reflection amplitudes intertwine with and partly overly the lower amplitude reflections of this unit (Fig. 4). U2 and the overlying unit U3 have similar reflection characteristics, but different reflection amplitudes (Fig. 2; Table 1).

4.2.4. Horizon R3 and unit U3

R3 highlights the transition from U2 into U3 (Figs. 3, 4 and 5a & b). This horizon is overall conformable to the underlying reflections of U2, but locally truncates U2 reflections, particularly at Site 2 (Figs. 3 and 4;

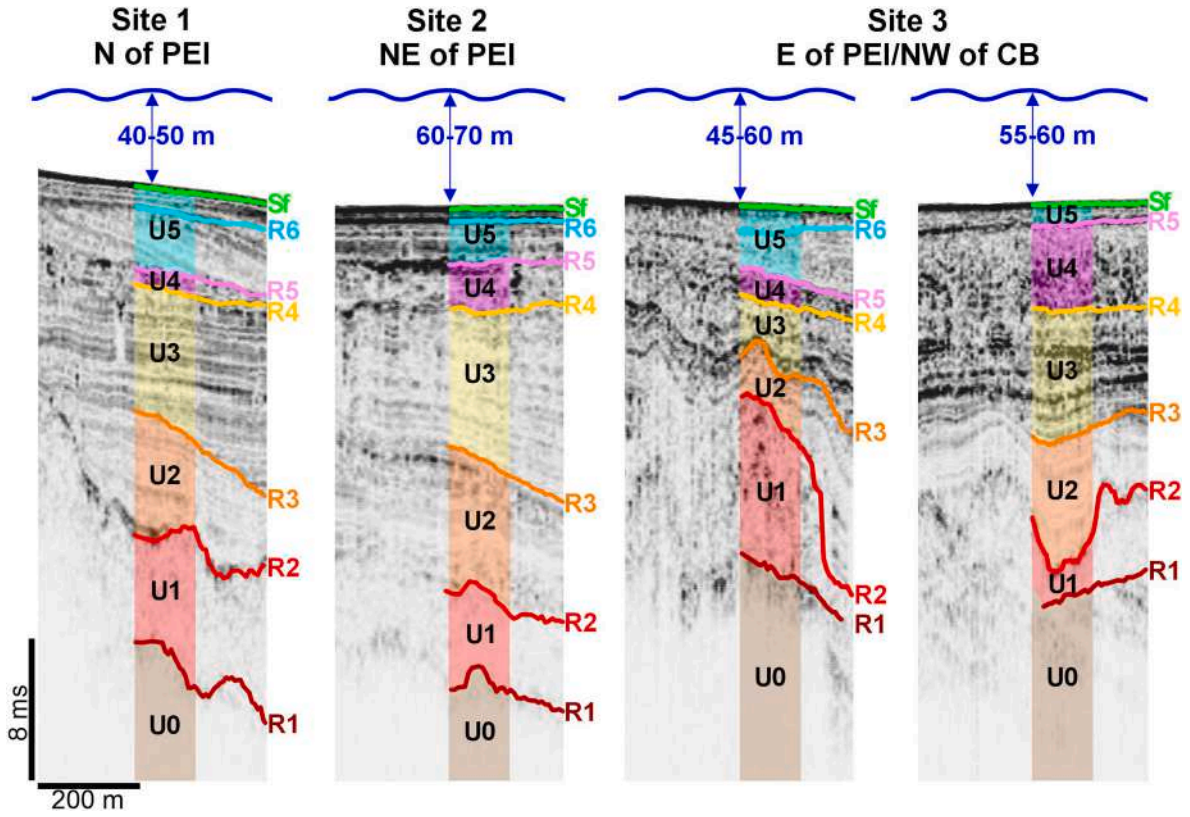

Fig. 2. Comparison of key acoustic reflections (R1-R6) and units (U0-U5) that were identified and mapped together with the seafloor reflection (Sf) within the three study sites (Site 1, 2 and 3). The reflections (R1-R6) are highlighted to the right, and acoustic units (U0-U5) are shown within the different colored boxes. All profiles have the same scale. The average water depth for each site is shown on top of each panel. Note that due to its size, we decided to show two examples for Site 3, which represent opposite shorelines located <20 km from the coasts of PEI and Cape Breton.

Table 1
Units and acoustic facies identified in the three study sites (Site 1, 2 and 3).

Unit	Examples	Description
Unit 5 (U5)	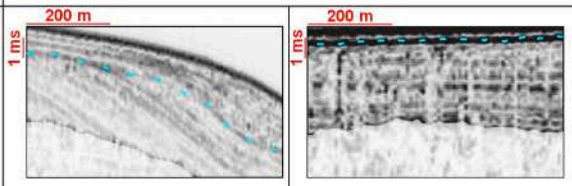	Distinct, coherent to incoherent, parallel and locally, intermittent sub-bottom reflections; separated by an unconformity (blue dots) into an upper (U5-a) and lower (U5-b) unit (1.5-9 ms/~1-7 m thick).
Unit 4 (U4)	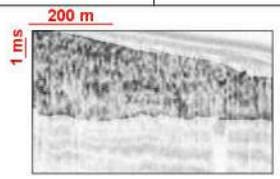	Incoherent internal reflections with at times indistinct, intermittent, parallel sub-bottom reflections (0.5-6 ms/~0.4-4.5 m thick).
Unit 3 (U3)		Distinct, coherent, parallel, generally high amplitude sub-bottom reflections; at times intermittent, indistinct reflections (2.5-36 ms/~2-27m thick).
Unit 2 (U2)	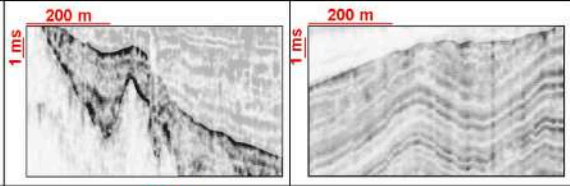	Distinct, coherent, parallel sub-bottom reflections at times intermittent; generally low amplitude, locally higher amplitudes; conform to U1 and variable in thickness (1.5-13 ms/~1-10 m thick).
Unit 1 (U1)	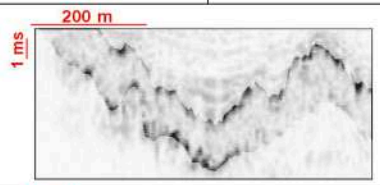	No apparent sub-bottom reflections (transparent); at times with incoherent, high amplitude internal character; often appears irregular/hummocky (2.5-12 ms/~2-9 m thick).
Unit 0 (U0)	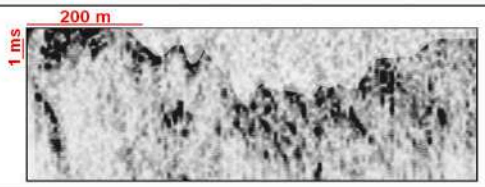	No sub-bottom reflections or high amplitude, incoherent, often gentle dipping sub-bottom reflections.

Table 1). R3 is often a coherent, high amplitude reflection at Sites 2 and 3, but it is partially absent, especially at Site 1 where R3 does not form a coherent reflection (Figs. 2–4, 5a & b). U3 is located on top of R3 and overall, 2.5–16 ms or ~2–12 m thick, except for Site 2 where it is up to 36 ms or ~27 m thick (Fig. 2, 4; Table 1). This unit shows high amplitude, coherent and in part intermittent, stratified reflections, which contrast with the generally low amplitude reflections of U2 (Fig. 2; Table 1). U3 reflections, which are often unconformable to U2 reflections, onlap horizon R3 (Fig. 2). Low amplitude to transparent, wedge-shaped features, and pockets are noticeable within U3, especially towards its top (Figs. 3 and 7). Distinct reflections are visible below these features (Fig. 7). At Site 1, we further observe dome-shaped features with low amplitude to no sub-bottom reflections within U2 and U3 (Fig. 3).

4.2.5. Horizon R4 and unit U4

R4 forms the top of U3 and base of unit U4 (Fig. 2). This horizon forms an erosional truncation to U3 reflections, especially at Site 1 and 2, but locally also appears conformable to the underlying reflections (Figs. 2–4; Table 1). The overlying unit U4 is of variable thickness in the range of 0.5–6 ms or ~0.4–4.5 m (Figs. 2 and 3). U4 shows primarily chaotic, high amplitude reflections with at times interbedded stratified, parallel reflections (Figs. 2–4; Table 1). A profile close to Cape Breton (Site 3) shows stratified reflections within U4, which downlap seaward on horizon R4 (Fig. 5b).

4.2.6. Horizon R5 and R6 and unit U5

R5 forms the top of U4 (Fig. 2) and generally appears undulated given the variations in thickness of the underlying unit (Figs. 3 and 5b). Unit U5 is located on top of R5 and is on average 1.5 ms or ~1 m thick at Site 1 and up to 9 ms or ~7 m thick at Sites 2 and 3. This unit consists of distinct, coherent and occasionally incoherent, parallel sub-bottom reflections (Fig. 2; Table 1). It can be subdivided into a lower (U5-a) and upper (U5-b) portion, which is separated by an internal high amplitude, often unconformable reflection named horizon R6 (Fig. 2; Table 1). The lower portion of U5 (U5-a) below R6 is usually >1.5 ms or >1 m thick. It

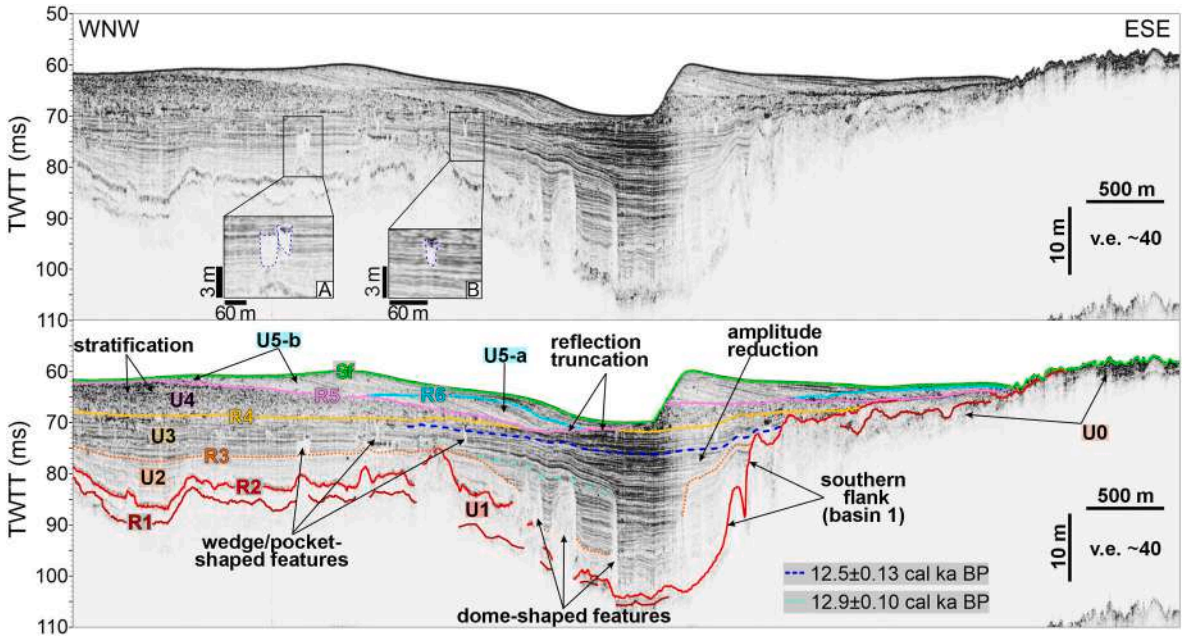

Fig. 3. WNW to ESE oriented sub-bottom profile acquired north of PEI (Site 1; see location in Fig. 1b and c). The top image shows the uninterpreted profile, while the bottom image shows the interpretation. Insets A) and B) in the top image show wedge-shaped features and pockets (blue dashed relief) that occur within U3. The distribution of key reflection horizons (R1-R6), acoustic units (U0-U5) and important reflection characteristics are highlighted. Radiocarbon ages from core GC07_2 are correlated to this profile (dashed blue and turquoise lines). (For interpretation of the references to color in this figure legend, the reader is referred to the Web version of this article.)

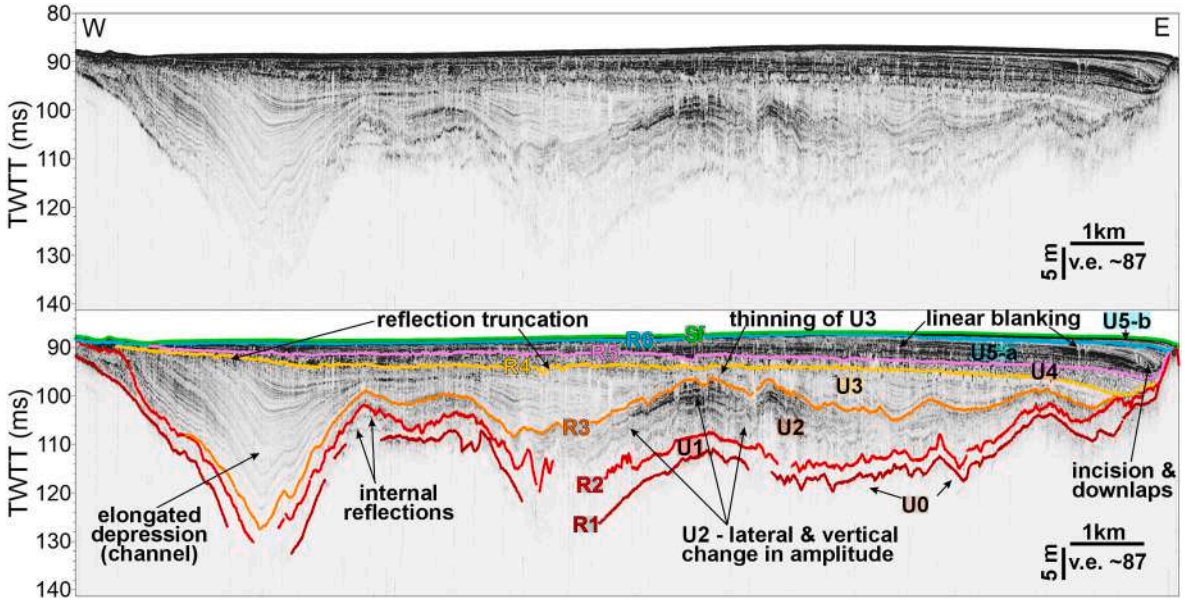

Fig. 4. W to E oriented sub-bottom profile acquired northeast of PEI (Site 2; see location in Fig. 1b). The top image shows the uninterpreted profile, while the bottom image shows the interpretation. The distribution of key reflection horizons (R1-R6), acoustic units (U0-U5) and important reflection characteristics are highlighted.

is, however, almost absent at Site 1, except for within the elongated seafloor depressions, where U5-a shows reflection downlaps (Fig. 3). At Site 2, U5-a reflection downlaps are associated with local, concave unconformities of various channel incisions (Fig. 4). The upper portion of U5 (U5-b) on top of R6 is more widely distributed than U5-a and usually forms a <1.5 ms or <1 m thick layer on top of U5-a or on top of U4 if U5-a is absent (Figs. 3, 4 and 5b). Within elongated depressions of Site 1, U5-b shows reflection downlaps like U5-a, but they are more gently inclined than those in U5-a (Fig. 3). Acoustic blank features are observed within U5 at Site 2, but in contrast to those observed within U3, linear acoustic blanking is apparent underneath these features (Fig. 4).

4.3. Reconstruction of paleosurfaces

Surface maps of reflection horizons, R1, R2, R4 and R5 provide insights into erosional and depositional changes within the study sites. R3 was not mappable for this purpose due to its partial absence, especially at Site 1. In addition, a surface grid of horizon R4 for Site 3 was not feasible, due to problems correlating between the widespread depressions with mappable reflection horizons that are separated by

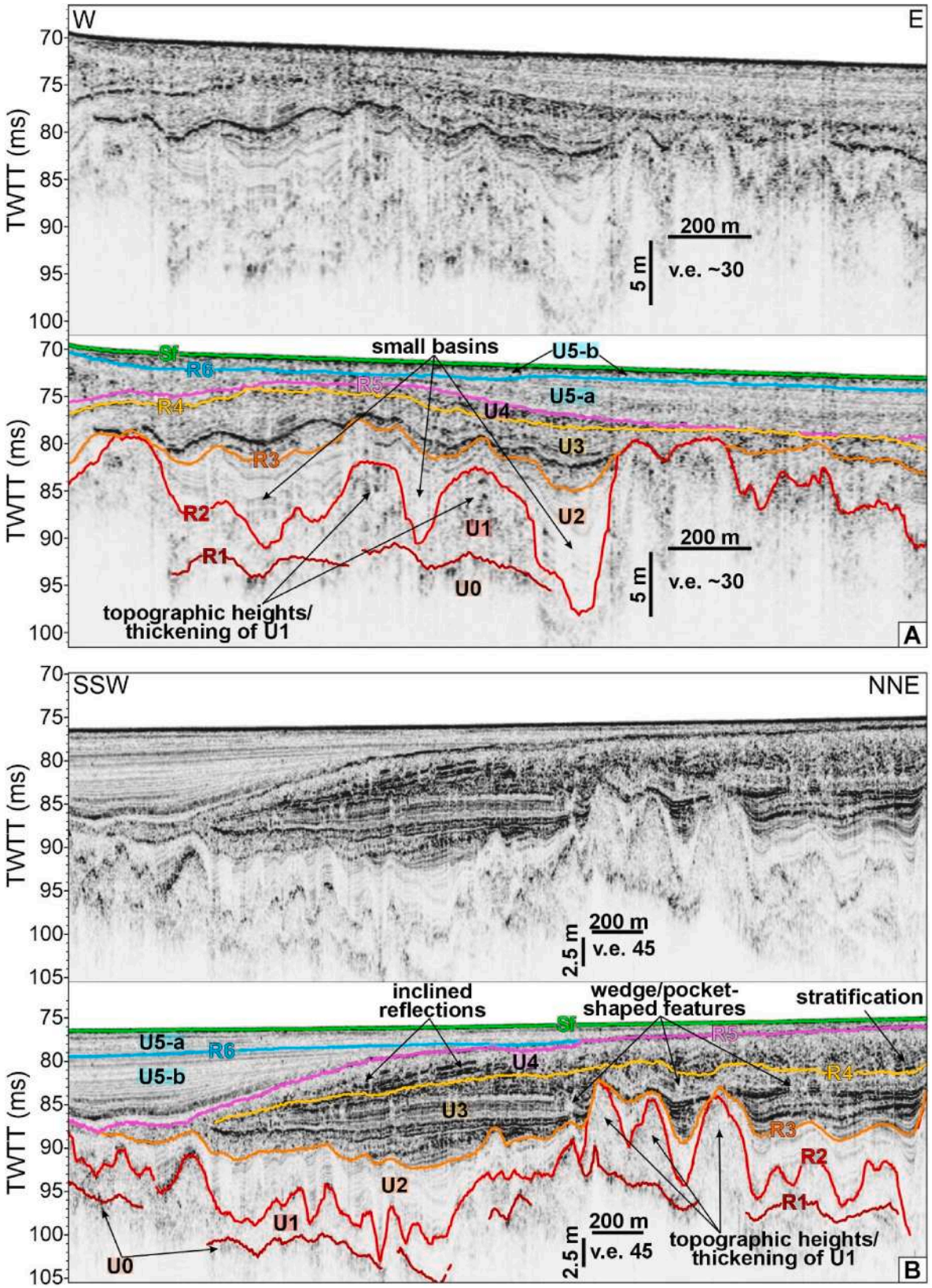

Fig. 5. A) W to E oriented sub-bottom profile acquired ~40 km offshore, east of PEI; and B) an SSW to NNE oriented sub-bottom profile acquired ~12 km off Cape Breton. In both cases, the top image shows the uninterpreted profile, while the bottom image shows the interpretation. The distribution of key reflection horizons (R1-R6) and acoustic units (U0-U5) as well as important reflection characteristics are highlighted. The location of the profiles is shown in Fig. 1b.

bedrock outcrops. Main morphological differences observed within each study site are presented in the following sections.

4.3.1. Morphological evolution of site 1

Grids of horizons R1 and R2 reveal two, 20–40 ms or ~15–30 m deep depressions resembling basins: a larger one (~29 km^2, basin 1) in the center of the study site and a small one (~4.5 km^2, basin 2) in its western portion (Fig. 6a). Basin 1 appears slightly elongated parallel to the present-day coastline of PEI (Fig. 6a). A noticeable 1 km wide, 8 km long and up to ~45 ms or ~35 m deep depression (7.4 km^2) is evident within basin 1 and extends parallel to its southern flank (Figs. 3 and 6a). In contrast to horizons R1 and R2, R4 shows an almost flat, seaward inclined topography, as both basins have been filled with U2 and U3 material (Figs. 3 and 6b). At horizon R5, several NNW-SSE-oriented, 4.5–19 ms or ~3.5–14 m deep, 0.8–1.3 km wide and 0.8–3.5 km long depressions are present in the central to eastern portions of the study site (Fig. S3). Most of these depressions are still observable along the present seafloor but are reduced to about half their size with their center being shifted northward after infill with U5 material (Fig. S3).

4.3.2. Morphological evolution of site 2

Surface maps of horizons R1 and R2 show three elongated NE- and EW-trending depressions that resemble channels (Fig. 4, 6c). The main system extends northeastward from the southwestern portion of Site 2, termed 'southern flank', and bifurcates into two, parallel extending NE-trending elongated depressions (Fig. 6c). An EW-trending elongated depression is also observed in the northern part of Site 2, which leads into the main, NE-oriented system of this site (Fig. 6c). The depressions at R1 are ~1.8 km wide with an incision depth between 13 and 40 ms or ~10 and 30 m (Fig. 6c). At R2 their width is reduced to ~1.4 km but with a similar incision depth (up to 40 ms or ~30 m) (Fig. S4). The NE-trending elongated depressions disappear at R4, while the EW-trending elongated depression is still present but notably reduced in width and depth e.g., from a width of 1.9 km with a depth of 20–33 ms or ~15–25

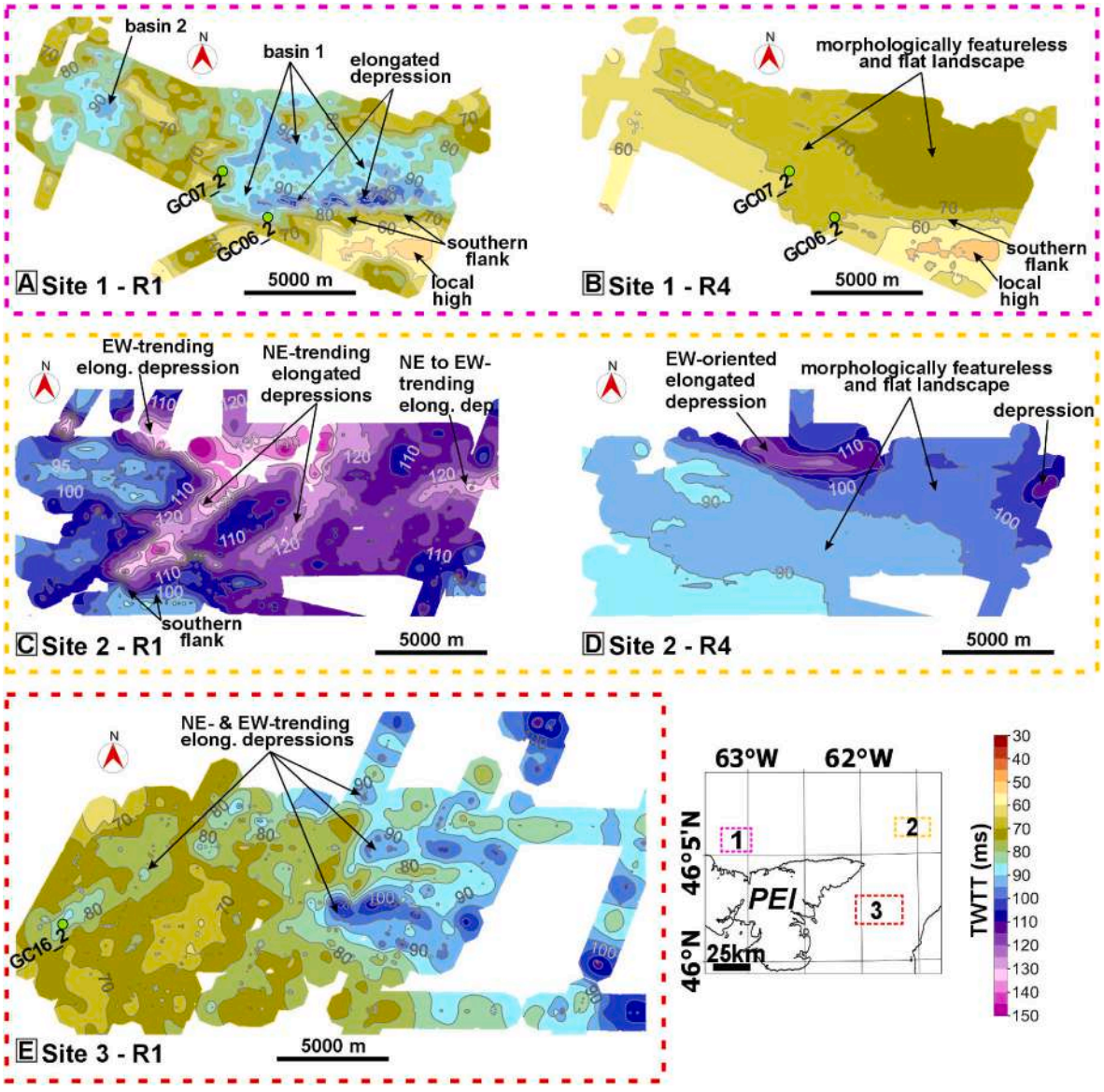

Fig. 6. Comparison of surface grids from the three study sites (Site 1, 2 & 3) in the Gulf of St. Lawrence showing the distribution of horizon R1 and R4 mapped using sub-bottom profiles. The overview map in the lower right corner shows the location of the three sites (dotted boxes 1, 2 & 3). Surface grids of horizon R1 and R4 are shown for Site 1 in panel A) and B) (pink box), Site 2 in panel C) and D) (yellow box), and of horizon R1 for Site 3 in panel E) (red box). Light green circles with black outlines show the location of sediment cores (GC06_2, GC07_2, GC16_2). (For interpretation of the references to color in this figure legend, the reader is referred to the Web version of this article.)

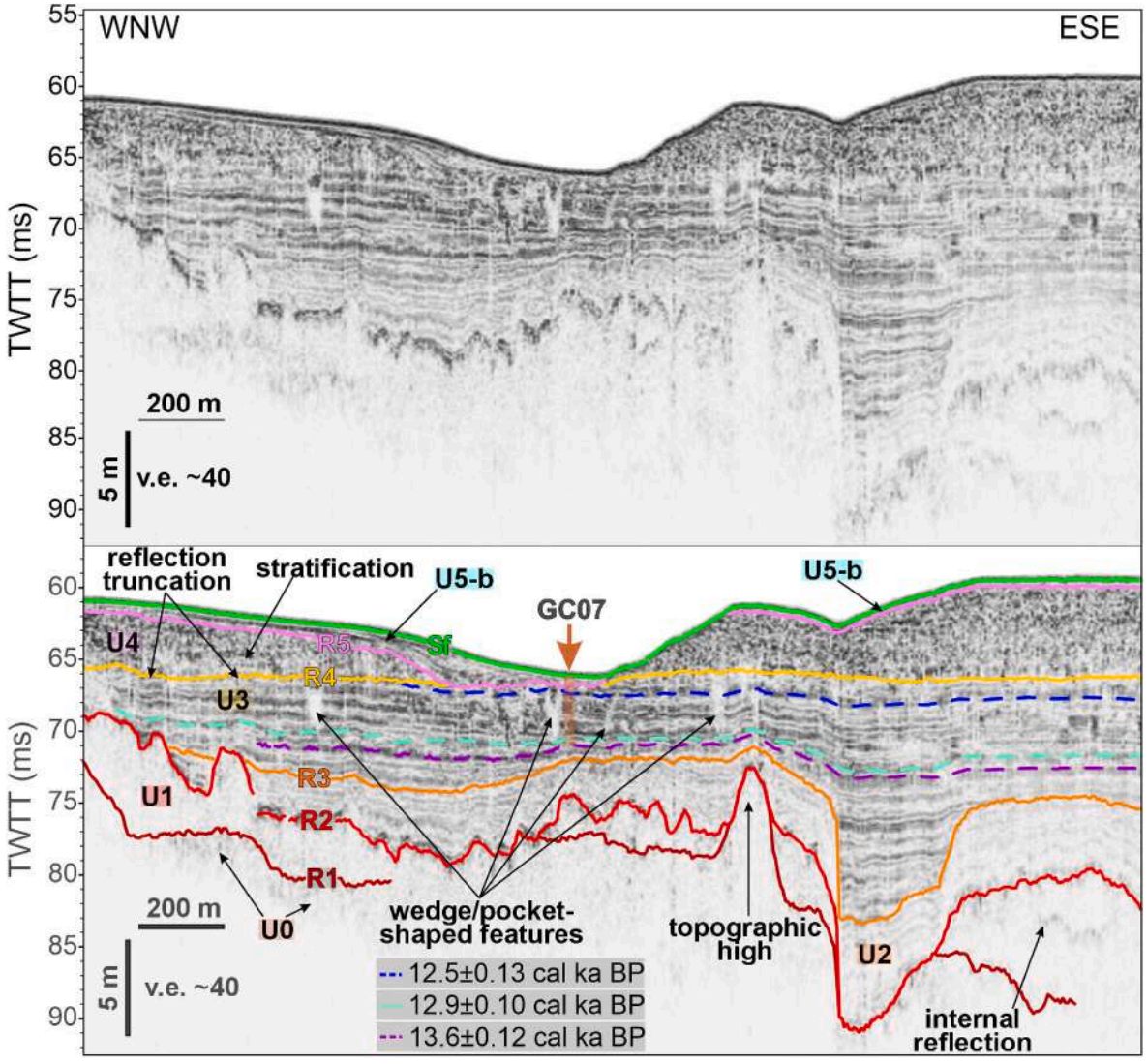

Fig. 7. Sub-bottom profile acquired north of PEI (Site 1, see location in Fig. 1b and c). The top image shows the uninterpreted profile, while the bottom image shows the interpretation with key reflection horizons (R1-R5) and acoustic units (U0-U5). Important reflection characteristics are highlighted. The location and depth of sediment core GC07_2 is shown (brown arrow and box), and the core stratigraphy was correlated to the sub-bottom profile (dashed blue, turquoise and lilac lines) with the corresponding age shown at the bottom. Note: horizon R6 is not shown as the lower portion of U5 (U5-a) is absent and its upper portion (U5-b) directly overlies U4. (For interpretation of the references to color in this figure legend, the reader is referred to the Web version of this article.)

m at horizon R2 to a width of 0.9 km and depth of 6–13 ms or ~5–10 m at horizon R4 (Fig. 6d). Like at Site 1, R4 appears slightly inclined seaward (Fig. 6d). The present seafloor shows no depressions or channels at Site 2, but EW-trending seafloor channels are present north of Site 2 (Fig. 1b–S1, S4).

4.3.3. Morphological evolution of site 3

Numerous NE to EW-trending, elongated depressions are present at Site 3 along horizons R1 and R2 (Fig. 6e). These horizons occur in 66–93 ms below sea level or ~50 to 60 mwd with 5–33 ms or ~4–25 m deep incisions (Fig. 6e). The EW-trending depressions extend from the coast of PEI and widen offshore where they are up to 2.8 km wide (Fig. 6e). The largest elongated depression is NS-trending, up to 45 ms or ~35 m deep and 6 km wide, and located proximally to Cape Breton (Fig. 6e). The depressions are still visible at horizon R2 but are reduced in size and the incision is shifted further offshore away from PEI (Fig. S5). From horizon R2 to the modern seafloor the depressions diminish in size and their incision is shifted further offshore (Figs. S2 and S5). No depressions or channels are visible along the modern seafloor east of PEI, as these are located further east and northeast of PEI (Fig. 1b–S2, S5).

4.4. Description of sediment cores

4.4.1. Sedimentological characteristics

4.4.1.1. Site 1. Two sediment cores (GC06_2, GC07_2) were collected within elongated seafloor depression where U4 and U5 are either absent or <30 cm thick (Figs. 1b and 7, S6). GC06_2 was retrieved from 49 mwd and is 3 m long, while GC07_2 was retrieved from 51 mwd and is 3.72 m long (Fig. 8). Between 3 and 0.2 m of GC06_2 and 3.72 to 0.22 m of GC07_2 both cores contain homogenous to massive dark reddish-brown to reddish-brown clay to clayey mud with traces of very fine to medium sand interbedded with layers of clay and silty sand (Fig. 8). Correlation of the cores to the sub-bottom profiles show that these sections of the cores (3–0.2 m of GC06_2, 3.72–0.22 m of GC07_2) sampled U3 (Fig. 7, S6). In contrast, the upper 0.2 m of GC06_2 and 0.22 m of GC07_2 consist of homogenous, dark brown to dark reddish-brown, medium to coarse sand with small amounts of gravel that either originate from U4 or U5 (Figs. 7 and 8, S6). Both cores contain intact shells and shell fragments (Fig. 8).

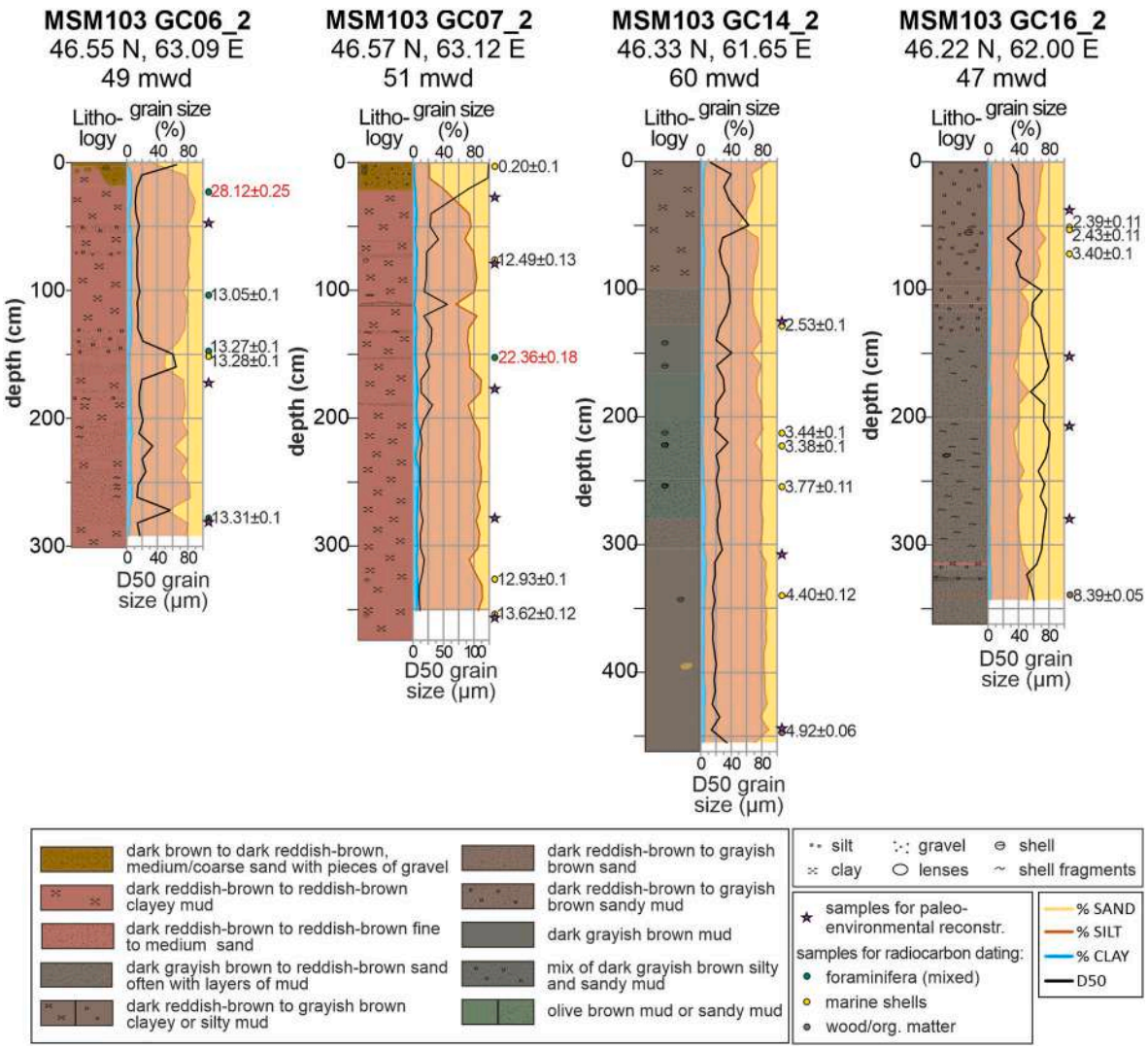

Fig. 8. Comparison of sediment core characteristics collected within the three study sites with GC06_2 and GC07_2 collected north (Site 1), and GC14_2 and GC16_2 collected east of PEI (Site 3). For each core the core lithology as well as measured percentage of clay, silt and sand, and median grain size (D50) in µm are shown. For details on the lithology see legend below; different colored dots next to the cores represent where samples for radiocarbon dating were extracted, while lilac stars show where samples for the biofacies analysis were extracted.

4.4.1.2. Site 3. Two sediment cores were collected at Site 3. GC14_2 was retrieved from 60 mwd about ~40 km offshore PEI and is 4.62 m long, while GC16_2 was retrieved ~20 km from shore in 47 mwd and is 3.62 m long (Figs. 1 and 8). GC14_2 consists of bioturbated, largely homogenous dark grayish brown to reddish-brown mud to silty mud and dark grayish brown sandy mud (Fig. 8). In contrast, GC16_2 contains bioturbated, homogenous dark grayish brown to reddish-brown sandy muds and silty muds with a higher amount of silt towards the top (Fig. 8). Correlations of GC14_2 and GC16_2 to sub-bottom profiles show that these cores retrieved sediments from U5. Shells and shell fragments of various species are abundant within both cores. The deeper core sections contain higher amounts of organic material, including wood and preserved plant remains.

4.4.2. Biofacies description

The foraminiferal assemblages include only benthic foraminifera with a generally good preservation state (Table S1; Supplementary Plates I & II). Biofacies from all samples were described, even if there was a low foraminifera abundance. The foraminifera in the cores are distinguished into three different biofacies (A, B, C), which are indicative of different environments.

1. Biofacies A is most common and was present within GC06_2, GC07_2, and in the lower part of GC16_2. This biofacies is dominated by the calcareous taxa *Elphidium excavatum* and *Elphidium clavatum*, along with *Haynesina orbicularis* and *Buccella frigida.*
2. Biofacies B only occurs in GC14_2 and is characterised by a generally poor assemblage, with *Nonionellina labradorica* and *Islandiella helenae* as relatively more frequent taxa, followed by *E. excavatum* and *E. clavatum.* Specimen tests occasionally show dissolution traces. Very rare specimens of the agglutinated taxa *Entzia macrescens, Lepidodeuterammina ochracea*, *Trochammina inflata* and *Trochammina squamata* are present, but given their very rare abundance we consider them as reworked.
3. Biofacies C is only found in the upper part of GC16_2 and is largely dominated by agglutinated taxa, namely *Lagenammina difflugiformis*, followed by scattered specimens of *Lagenammina atlantica* and rare, or very rare, specimens of *E. excavatum* and *B. frigida.* The distinction between *L. atlantica* and *L. difflugiformis* can be challenging, but *L. atlantica* typically lacks a developed neck present in *L. difflugiformis* (cf. Todd and Low, 1981).

4.4.3. Geochronology and sedimentation rates

Of the 20 samples extracted for radiocarbon dating, two, GC06_2(a) and GC07_2(c), yielded inverse ages suggesting that sediment was reworked and, therefore, were not considered in the age models and to calculate sedimentation rates (Table 2).

Sediment cores from Site 1 (GC06_2, GC07_2) that sampled U3 have calibrated ages from ~13.6 ± 0.12 to 12.5 ± 0.13 ka cal BP, which would correspond to the late Bølling-Allerød (13.6–12.9 ka cal BP) and early Younger Dryas (12.9–12.5 ka cal BP) (Fig. 8; Table 2). These dates are calibrated using a modern correction factor for the marine reservoir effect (ΔR-83 ± 50 a, McNeely et al., 2006). Studies on other former glaciated regions, such as Quebec and the Gulf of Maine, however, used a ΔR of 600 ± 150 a for >10 ka old samples (Borns et al., 2004; Tremblay and Lamothe, 2007 as cited in Thompson et al., 2011). Applying this ΔR suggests a later deposition of U3, between the early Younger Dryas and early Holocene (~12.8 ± 0.18–11.3 ± 0.26 ka cal BP) (Table S2). To estimate sedimentation rates within the deeper basin sections we correlated the core stratigraphy to sub-bottom profiles (Figs. 3 and 7, see Fig. S7 for cores). In basin 1 at Site 1, the apparent late Bølling-Allerød or early Younger Dryas time interval, which spans ~700 a, is up to 3 m thick, yielding a sedimentation rate of up to 0.4 cm a^{-1} (Table 2). The overlying stratigraphy, which is up to 5 m thick and deposited either over ~460 a of the early Younger Dryas or 790 a of the Younger Dryas to Holocene period (Figs. 3 and 7; Table 2, S2), suggests sedimentation rates of 1 or 0.6 cm a^{-1}, respectively.

Sediment cores collected at Site 3 (GC14_2, GC16_2) date within the Holocene (8.4 ± 0.06–2.3 ± 0.11 ka BP) (Fig. 8, Table 2). In all cases, the sampled sections correspond to U5 (Fig. 5a). For GC14_2 (Site 3), which is 4.5 m long and is dated to the late Holocene (4.9 ± 0.06–2.5 ± 0.10ka cal BP), we can calculate sedimentation rates between 0.2 and 0.09 cm a^{-1} with a decrease towards the top of the core (Fig. 1b and 8, S7). In comparison, sedimentation rates of 0.07 and 0.05 cm a^{-1} can be derived for GC16_2 (Site 3) for the past 8 ka (Fig. 1b–S7). These findings indicate high sedimentation rates for the Bølling-Allerød and Younger Dryas event (0.4–1 cm a^{-1}) and low sedimentation rates during the Holocene (0.05–0.2 cm a^{-1}).

5. Discussion

5.1. Bedrock geomorphology

U0 is present throughout all study sites, and often shows dipping sub-bottom reflections, especially to the east of PEI (Site 3) (Fig. 2, Table 1). We interpret U0 as representative of bedrock (Fig. 9), which in the Maritime Basin are represented by the Carboniferous to Permian sandstones that are often described as flat dipping (Carr, 1969; Symons, 1990; Van de Poll, 1989). Horizon R1 forms the boundary between these "redbeds" and the overlying unconsolidated sediments (Fig. 2). Mapping of R1 exposes various, presently buried depressions within the bedrock (Fig. 6a, c & e, 9). The up to 35 m deep depressions to the north of PEI (Site 1) resemble isolated basins, given their lack of continuity within the survey area (Figs. 3 and 6a). They are oriented parallel to the modern PEI coastline and within these basins several topographic elevations are observable (Figs. 3 and 6a). Given these characteristics, it is possible that the basins were formed by glacial erosion (Fig. 9) (cf. Cook and Swift, 2012; Patton et al., 2016). To the east (Site 3) and especially northeast of PEI (Site 2), R1 reveals numerous EW- to NE-trending elongated depressions within the bedrock, which resemble channels with some being directed towards the CBT (Fig. 1a & b, 6c & e). Channels observed at Site 2 occur in fact in vicinity to present-day EW-oriented seafloor channels

Table 2
Sediment samples and determined calibrated ages. Marked in red are dates that differ significantly from the other samples (above and below) and, therefore, were not considered further, such as for calculation of the sedimentation rates.

core name	sample name	depth (cm)	sample material	lab nr.	^{14}C a BP ± 1 σ	2 σ range cal. ages (cal a BP) (95 %)	average age (cal a BP)
GC06_2	a	23.0	foraminifera (mix)	Poz-171626	24,710 ± 190	28,598 - 27,695	28,115 ± 240
	b	104.0	foraminifera (mix)	Poz-171627	11,650 ± 60	13,269 - 12,839	13,051 ± 106
	c	148.0	foraminifera (mix)	Poz-171629	11,870 ± 60	13,481 - 13,085	13,273 ± 103
	d	152.0	marine shell	Poz-171630	11,880 ± 60	13,492 - 13,091	13,283 ± 104
	e	279.0	foraminifera (mix)	Poz-171631	11,910 ± 70	13,552 - 13,101	13,314 ± 111
GC07_2	a	3.0	marine shell	Poz-172453	665 ± 30	400 - 17	201 ± 93
	b	76.5	marine shell	Poz-171632	10,990 ± 50	12,660 - 12,180	12,438 ± 128
	c	153.0	foraminifera (mix)	Poz-171633	19,190 ± 120	22,740 - 22,034	22,357 ± 175
	d	327.0	marine shell	Poz-171634	11,520 ± 60	13,117 - 12,733	12,925 ± 100
	e	354.5	marine shell	Poz-171635	12,190 ± 60	13,876 - 13,390	13,623 ± 118
GC14_2	a	128.0	marine shell	Poz-171639	2,850 ± 30	2,724 - 2,344	2,532 ± 103
	b	213.0	marine shell	Poz-171640	3,610 ± 35	3,665 - 3,250	3,444 ± 100
	c	223.0	marine shell	Poz-171641	3,555 ± 30	3,574 - 3,189	3,378 ± 97
	d	255.0	marine shell	Poz-171689	3,875 ± 35	3,999 - 3,561	3,772 ± 110
	e	342.0	marine shell	Poz-171691	4,350 ± 35	4,642 - 4,179	4,404 ± 115
	f	448.0	wood fragment	Poz-172073	4,350 ± 40	5,040 - 4,841	4,921 ± 59
GC16_2	a	51.0	marine shell	Poz-171692	2,735 ± 35	2,638 - 2,176	2,390 ± 113
	b	53.0	marine shell	Poz-171693	2,765 ± 35	2,676 - 2,228	2,429 ± 111
	c	72.0	marine shell	Poz-171695	3,570 ± 35	3,606 - 3,209	3,396 ± 100
	d	399.5	org. sediment	Poz-172072	7,580 ± 50	8,519 - 8,212	8,385 ± 52
Indices:			Reservoir corr. marine samples: -83±50 a (modern corr. factor)				

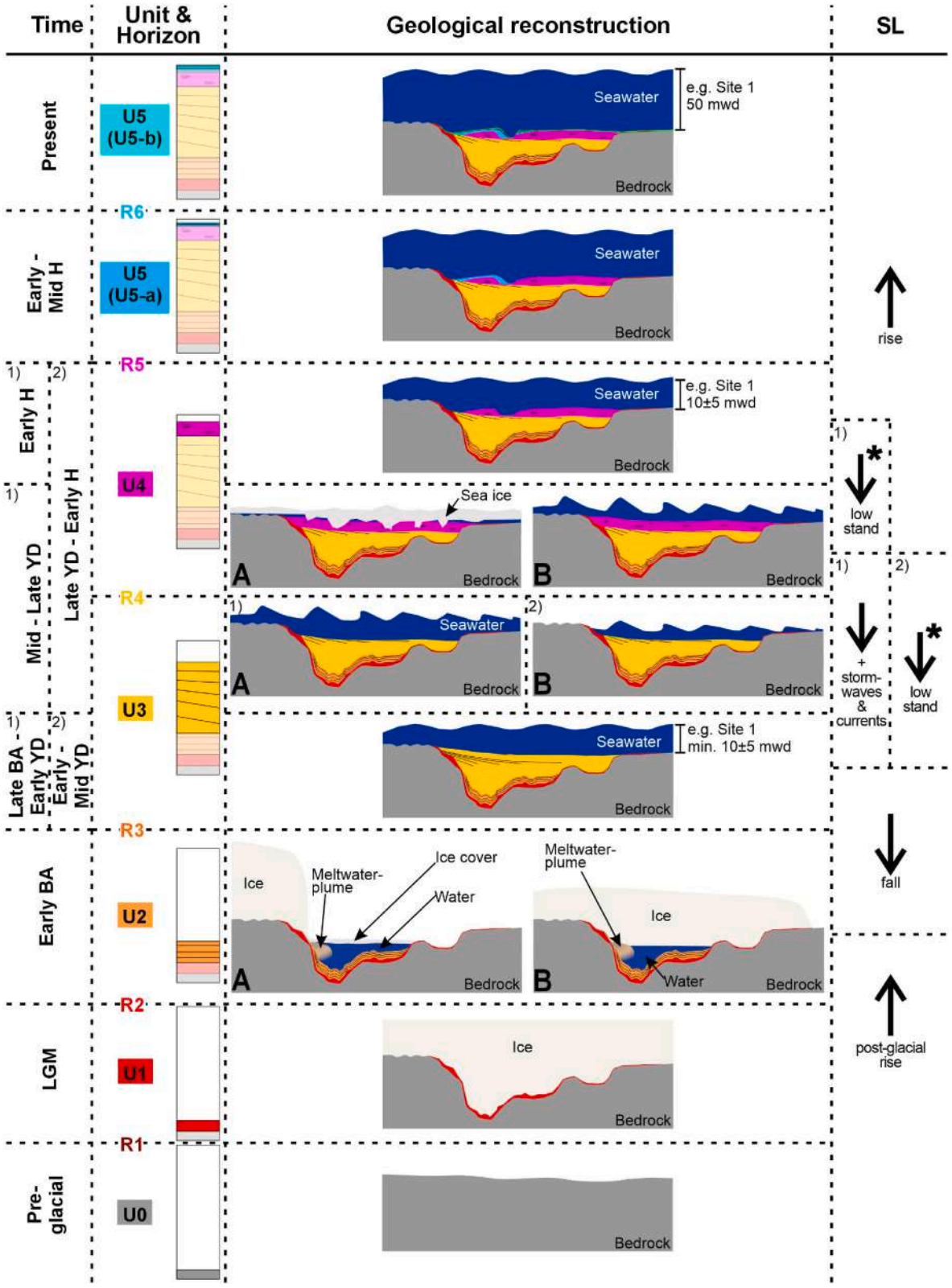

Fig. 9. Geological reconstruction of the stratigraphic and sedimentological evolution of the study area from the LGM to present. Acronyms are as follow: LGM = Last Glacial Maximum, BA = Bølling-Allerød, YD = Younger Dryas, and H = Holocene. Small numbers in the upper left corners of units indicate different possible interpretations with 1) using ΔR-83 ± 50 a, and 2) using ΔR600 ± 150 a. A and B panels represent different interpretations for the deposition of U2, U3 and U4. SL stands for estimated sea level development and arrows indicate the apparent change in relative sea level. Arrows with a star represent a RSL lowstand described also by Shaw (2005), Forbes et al. (2014) and Vacchi et al. (2018).

located between PEI and the Magdalen Islands (Fig. 1b), which were previously interpreted as tunnel valleys (Loring and Nota, 1973). It is thus plausible that the presently buried channel systems observed at Sites 2 and 3 are remains of tunnel valleys (cf. Loring and Nota, 1973; Shaw et al., 2006; Pinet and Brake, 2024) or lowstand, fluvial river systems (Fig. 9) (cf. Pinet and Brake, 2024).

5.2. Late Pleistocene and Holocene depositional reconstruction

5.2.1. Last Glacial Maximum

U1 is the lowermost depositional unit within all basins and channels in the research area (Fig. 2). Given the acoustic response of U1 (transparent with no apparent sub-bottom reflections) and its variable thickness (2–9 m thick) distribution we interpret this unit as glacial till (cf. Josenhans et al., 1986; Josenhans and Fader, 1989; Zecchin and Rebesco, 2018) (Figs. 2, 5 and 9, Table 1), which was likely deposited when the LIS occupied the Gulf of St. Lawrence (Loring and Nota, 1973). The glacial till (U1) directly overlies the bedrock (R1, U0) (Fig. 2), which indicates that the ice was grounded during deposition of U1 within the basins and channels (Josenhans and Lehman, 1999; Shaw et al., 2006), and supports the interpretation that these basins and channels were indeed formed from subglacial erosion and by meltwater flows (Fig. 9) (cf. Loring and Nota, 1973; Cook and Swift, 2012; Patton et al., 2016). Basins and channels are still evident within horizon R2 (Figs. 3 and 4), although their width is reduced due to the infill with glacial till (Figs. S3, S4, S5).

5.2.2. Bølling-Allerød and Younger Dryas

The stratified nature of U2 and U3, and association of U3 reflection characteristics to clayey mud with interbedded sand (GC06_2, GC07_2) on top of U1 suggests that these units represent glaciolacustrine, glaciomarine or marine sediments (Figs. 3, 7 and 8) (cf. Josenhans et al., 1986; Josenhans and Fader, 1989; Zecchin et al., 2016). Radiocarbon dating indicates the sampled section of U3 as of late Bølling-Allerød to early Younger Dryas (13.6 ± 0.12–12.5 ± 0.13 ka cal BP) to potentially early Holocene (11.3 ± 0.26 ka cal BP) age (Fig. 7; Table 2, S2). It needs to be noted, however, that sub-bottom profiles show a significant thick section of U3 within deeper basins below the lowermost dated section, potentially indicating high sedimentation rates throughout its deposition (Figs. 3 and 7). Using a ΔR of 600 ± 150 a, this lowermost dated portion would have been deposited during the early Younger Dryas (>12.8 ± 0.18 ka cal BP; Table S2), which indicates that deposition of U3 began earlier, during the late Bølling-Allerød. Consequently, the deposition of U2, not dated directly, places after the LGM and before the late Bølling-Allerød, and thus likely within the early Bølling-Allerød, as described in the following section.

5.2.2.1. Early Bølling-Allerød. U2 shows conformable, low amplitude reflection characteristics (Table 1). Sediments with such a seismic response have been interpreted elsewhere as ice proximal to distal glaciolacustrine or glaciomarine mud with layers of ice rafted debris that were deposited within a low-energy environment, primarily from suspension clouds in association with sediment-laden meltwater or hyperpycnal flows (e.g., Josenhans and Fader, 1989; Josenhans et al., 1990; García-García et al., 2004; Zecchin and Rebesco, 2018; Hogan et al., 2020; Dhavamani et al., 2022).

The age constraint and distribution of U2 within deeper portions of basins and channels (15–35 m deep) suggest that low-lying regions of the shelf were flooded with meltwater during the ice retreat (Figs. 4, 7 and 9). Given the strong conformity of U2 reflections to horizon R2, these portions of the shelf were likely covered by sea ice or ice remnants, which facilitated the formation of a low-energy and sheltered environment (Figs. 4 and 5a & b, 7, 9). A similar conformable acoustic unit was observed in basins along the inner Scotian Shelf and attributed to rapid sedimentation from suspension clouds and meltwater underneath an ice shelf in the ice-proximal portion (e.g., Stea et al., 1996). Changes in the reflection amplitude of U2 observed within channels at Site 2 (Fig. 4, Table 1), indicate lithological changes and are likely related to changes in the amount of ice rafted debris, as Site 2 is located further offshore and was possible affected by ice retreat and RSL rise at an earlier stage during deglaciation (c.f. Josenhans et al., 1990; Melles and Kuhn, 1993; Hodell et al., 2010; Batchelor et al., 2011; Klotsko et al., 2019). Marine water was likely present during the deposition of U2 given the rapid post-glacial rise in RSL (Fig. 9) (e.g., as suggested by Shaw et al., 2002; Shaw, 2005; Dyke et al., 2003; Forbes et al., 2014; Dalton et al., 2020). An unconformity at the top of U2 (horizon R3) indicates a change in the depositional environment or in the intensity of marine processes (Figs. 3 and 7) (cf. Mitchum Jr. et al., 1977).

5.2.2.2. Late Bølling-Allerød and Younger Dryas. U3 has a similar reflection character as U2 (Table 1). Sediment cores (GC06_2, GC07_2) from U3 consist of dark reddish-brown clayey mud interbedded with layers of fine and medium sand (Fig. 8). The abundance of fine-grained material suggests deposition under generally low-energy conditions within an environment that periodically experienced higher energy events, as indicated by the presence of sandy layers (Zecchin et al., 2016; Zecchin and Rebesco, 2018). These findings correspond to the abundance of taxa from biofacies A that are related to marginal marine, open bay settings (*E. excavatum*, *E. clavatum*, *B. frigida*) as well as shallow marine arctic and ice-proximal conditions with variable salinity and sediment supply (e.g., Schafer and Cole, 1982; Scott et al., 1977, 1980, 2001; Rodrigues and Hooper, 1982; Hald and Korsun, 1997). Sub-bottom profiles further indicate an increase in sedimentation rates towards the top of U3 from ~0.4 cm a^{-1} to ~1 cm a^{-1} or, given the uncertainty in age, 0.6 cm a^{-1}.

Sedimentation rates during the late Bølling-Allerød in the lower to middle portion of U3 are relatively high considering present-day rates of <0.2 cm a^{-1} and are possibly related to an increase in wave and current energy due to the absence of ice coverage, which we also interpret as the primarily cause for the unconformity at horizon R3 (Figs. 4 and 9) (c.f., Barrie and Piper, 1982; Stea et al., 1996). The shift to higher sedimentation rates towards the top of U3, that is associated with the Younger Dryas event, indicates a change in the depositional conditions. In this context, Loring and Nota (1973) who analyzed glaciomarine sediments from the St. Lawrence Estuary and Laurentian Channel argued that higher sedimentation rates during the Younger Dryas event were directly related to sedimentation in front of re-advancing ice masses. While the extent of a Younger Dryas ice mass is a matter of debate (Stea and Mott, 1998), the distribution and age of U3 suggests that deteriorating conditions with possible increased storm activity and sea ice development caused a transition to higher sedimentation rates in the research area (cf. Stea et al., 1996, 1998).

The top of U3 (horizon R4) shows an erosional truncation (Fig. 6b & d, 9) that is inclined seaward and could be generated by: 1) erosion due to intensified storm-wave activity during the Younger Dryas (Fig. 9) (cf. Barrie and Piper, 1982; Stea et al., 1996; Brauer et al., 2008; Słowiński et al., 2017), possibly amplified by sea level fall either related to isostatic rebound of the region (e.g., as suggested by Shaw et al., 2002; Shaw, 2005; Dyke et al., 2003), or ice build-up as proposed for other margins (Maselli et al., 2011). Alternatively, the truncation could be caused by 2) a RSL lowstand, which is argued to have occurred in this region during the late Pleistocene to early Holocene transition as a result of isostatic uplift following the ice retreat (Forbes et al., 2004; Shaw et al., 2006; Vacchi et al., 2018).

An erosional truncation has also been associated with a Younger Dryas sediment unit observed within basins on the inner Scotian Shelf (Piper and Fehr, 1991; Stea et al., 1996). Contrary to our data, however, these units interpreted to be of Younger Dryas age were found above a truncation, which would coincide with U4 in our data. Given the uncertainties in the dating and absence of dated material in the overlying

sediment unit (U4), we are unable to clearly determine the exact cause and timing for the formation of the erosional truncation atop the Younger Dryas sediments (U4, horizon R4) (Figs. 3 and 6b & d, 9).

5.2.3. Younger Dryas – Holocene transition

The echo characteristic of U4 (chaotic with interbedded parallel reflections) strongly contrasts with those of U3 (Fig. 2, Table 1). Papatheodorou et al. (2021) observed a similar echo-characteristic to U4 in the central Ionian Sea and interpreted them as a result of soft-sediment deformation. There is, however, no definitive sediment sample from U4, as the medium to coarse sand with pieces of gravel at the tops of GC06_2 and GC07_2 could be sediment material from either U4 or U5 (Figs. 7 and 8).

Radiocarbon dating of the units below and above U4 suggests a deposition of this unit after 12.5 ka cal BP and before 9 ka cal BP (Fig. 7; Table 2, S2). This time interval envelopes the Younger Dryas event, which likely saw an ice re-advance from isolated marine and terrestrial ice remnants on PEI and Nova Scotia (Stea and Mott, 1989, 2005; Shaw et al., 2006; Stea, 2011; Vacchi et al., 2018; Dalton et al., 2024). An absence of geological features such as moraines, drumlins or eskers along horizons R4 and R5, however, indicates that there was no grounded ice mass in our study sites (cf. Shaw, 2005; Shaw et al., 2006, 2009). Near the coast of Cape Breton, we observe inclined sediment layers at the base of U4 lapping down on horizon R4, creating a wedge-shaped geometry, but which laterally and at shallower elevations transition to the chaotic echo signature of U4 (Fig. 5b–S8). These characteristics resemble attributes of subaqueous fans formed in front of the grounding line of floating ice or glaciers (Dowdeswell and Fugelli, 2012) but could also constitute the distal component of a flood delta.

Based on the above information, we propose two hypotheses for the deposition and chaotic reflection characteristic of U4 (Figs. 3, 7 and 9; Table 1).

1) If R4 was caused by increased storm-wave activity, possibly accompanied by a RSL fall, during the Younger Dryas, then U4 likely resulted from meltwater-derived sedimentation in front of a new ice margin on PEI or underneath sea ice formed during the Younger Dryas (Fig. 9). Waves and tides, enhanced by the intensification of winds and storms during the Younger Dryas (Fig. 9) (cf. Brauer et al., 2008; Toomey et al., 2017), could have deposited and continuously reworked U4 sediments causing the chaotic appearance of this unit (cf. Forbes et al., 2014). Alternatively, sea ice could have invoked sediment disturbance through freezing and subsequent shearing of the upper sediment strata (Fig. 9). Present-day multi-year sea ice in Antarctica is up to 10 m thick as a result of ice deformation (Goosse et al., 2013), which implies that Younger Dryas sea ice offshore of PEI could have potentially been in direct contact with the sediments proximal to the coast especially if the RSL had dropped. It further suggests that the wedge-shaped depositional pattern observed offshore Cape Breton could be a direct consequence of sedimentation underneath floating ice near the coast (Fig. 5b–S8). In this scenario, the undulating surface of U4 (horizon R5) could possibly be an erosional truncation related to the sea level lowstand during the late Pleistocene to early Holocene transition (Figs. 3 and 9).
2) Another possible explanation would be that U4 deposited in the vicinity of the coastline, if the erosional truncation at horizon R4 is indeed related to the late Pleistocene to early Holocene RSL lowstand (Fig. 9). This unit was deposited on top of U3 and is therefore located in a shallower water depth than the older sediment units (Fig. 2; Table 1). We thus suggest that waves and tide action deposited and continuously reworked U4 (Fig. 9) (cf. Forbes et al., 2014). This scenario supports the idea that the observed wedge could be a relict flood delta into shallow water. Given this scenario, the undulating appearance of horizon R5 is either a consequence of thickness variations of U4 or related to erosion due to sea level rise at the end of the lowstand (Fig. 9). Determining the nature of the unconformity at horizon R5 is difficult, as the chaotic appearance of the upper part of U4 restricts the identification of reflection truncations (Table 1).

Both hypotheses seem to be feasible according to the available data, but the nature of U4 will need to be re-evaluated with actual samples from this unit in the future.

5.2.4. Holocene sedimentation

U5 consists of fine-to coarse-grained sandy mud and muddy sand of Holocene age (11.6 ka BP to present) (Fig. 8; Table 2). The lower portion or U5-a is up to 4 m thick and is present within elongated depressions (Site 1) and channels (Site 2 & 3), while the upper portion or U5-b is only 0.5–1 m thick but present throughout the research area (Figs. 3 and 5b). U5 overall displays parallel, stratified reflections (Fig. 2). Exceptions are found north of PEI (Site 1) and locally northeast of PEI (Site 2). North of PEI (Site 1), U5 migrates into and abruptly terminates within the elongated depressions present along the modern seafloor (Fig. 1c and 3). The unit shows reflection downlaps, which resemble sediment drifts from bottom currents observed in other areas such as the Barents Sea (Zecchin et al., 2016; Rebesco et al., 2016). Northeast of PEI (Site 2) but only within U5-a, localised reflection downlaps are observable that are associated with buried channel structures (Fig. 4). These channels occur in higher water depth (90 mwd) than sediment drifts observed to the north of PEI (50 mwd) (Fig. 1b). The acoustic response within U5-a resembles multicycle incisions found within former meandering channel systems or erosional channel belts (cf. Janocko et al., 2013; Dubey et al., 2019). They are often associated with sea level fluctuations and consequent changes in the hydraulic energy condition (Janocko et al., 2013; Dubey et al., 2019).

Sediment cores from U5 contain biofacies A (lower part of GC16_2), B (GC14_2) and C (upper part of GC16_2) and indicate a similar depositional trend than described above (Table S1). The taxa suggest a shift from shallow marine conditions (*E. excavatum*, *E. clavatum*, *B. frigida*, Rodrigues and Hooper, 1982; Schafer and Cole, 1982; Scott et al., 1977, 1980, 2001) during the early Holocene to conditions with strong salinity and temperature gradients during the late Holocene (*L. atlantica* previously known as *Saccamina atlantica,* Williamson et al., 1984). The late Holocene taxa further indicate a high flux of organic matter and is dominated by taxa associated with cold and well oxygenated bottom water (*L. difflugiformis* in biofacies C, Vilks et al., 1982; Jennings and Helgadottir, 1994; Alve et al., 2016) <20 km from PEI (GC16_2) and low oxygen conditions further offshore (>20 km) (GC14_2, *N. labradorica* & *I. helenae* of biofacies B, Hald and Korsun, 1997; Bernhard and Bowser, 1999; Rytter et al., 2002; Cage et al., 2021; Schmidt et al., 2022; Racine et al., 2023).

In conclusion, the topmost sediment unit, U5, shows both Holocene drift deposits strongly influenced by bottom, or in this case more likely coastal, currents in the shallower parts of the shelf and localised occurrence of multicycle, buried channel systems in the deeper, eastern sections of the research area (Figs. 3 and 4). A change in the environment conditions is further evident through the occurrence of an unconformity (horizon R6) within U5 (Fig. 3; Table 1), probably in response to Holocene sea level fluctuations (cf. Forbes et al., 2004, 2014; Shaw et al., 2006). U5-a was likely deposited during the early Holocene when the sea level rose rapidly, while U5-b was deposited more recently during lower rates of sea level rise (Fig. 9) (cf. Forbes et al., 2004, 2014).

5.3. Specific depositional or post-depositional formations

Transparent, wedge- and pocket shaped features that we observed within U3 (Figs. 3, 5 and 7) are potentially associated with rapid sedimentation of this unit given that similar features are described in association with cut and fill and sediment loading elsewhere (e.g., Kleiber et al., 2001; Fulthorpe and Austin Jr, 2004; Correggiari et al., 2005). Acoustic blanking can, nevertheless, also be an indication for the presence of a significant (>2 % of pore space) amount of free gas in

sediments (Lohrberg et al., 2020). Such gas accumulations, which may be produced by *in situ* degradation of organic matter in the presence of low permeability, however, absorb the seismic signal generating acoustic blanking of layers underneath, but this is not the case here (Figs. 3 and 7). Transparent, funnel-shaped features that resemble our wedge-shaped features have further been reported offshore New Zealand and interpreted as buried pockmarks that were formed by vertical fluid flow (Micallef et al., 2022). Interestingly, we observe dome-shaped features with low amplitude to no sub-bottom reflections in sub-bottom profiles north of PEI (Site 1), in vicinity to the wedge-shaped features of U3 (Fig. 3). These dome-shaped features resemble fluid plumes observed in sub-bottom profiles and seismic reflection profiles elsewhere (e.g., Trincardi et al., 2004; Lundmark, 2017; Papatheodorou et al., 2021), which may indicate that both, wedge-shaped and dome-shaped features, may have resulted from similar mechanisms.

Fluid plumes described in the literature, however, often extend through the sediment package to the seafloor. The funnel-shaped features observed offshore New Zealand further show a much larger size with >50 m vertical extension and lateral amplitude reductions underneath these features are noticeable (Micallef et al., 2022), which is different to the ones observed in our study within U3 (<5 m high). They, however, resemble acoustic blank features observed within Holocene sediments (U5) deposited northeast of PEI (Site 2) (Fig. 4). We, therefore, interpret wedge-shaped features observed within U5 at Site 2 as result of fluid expulsion, potentially consisting of gas, while those in U3 are either a direct result of rapid sediment deposition or also fluid expulsion, but its unclear if this is gas related. Coincidently, the dome-shaped features are likely related to fluid expulsion, but at this stage further data and analysis are needed to indicate the nature of these dome-shaped features.

5.4. Indications of ice advance and retreat and the influence on sea level

Based on the distribution of reflection characteristics and results from our sediment core analysis, we propose a modified deglaciation model for our research area for the last 18 ka BP (sections 5.1 and 5.2) by adding our findings to previous regional reconstructions such as those by Dyke et al. (2003), Shaw et al. (2006), Vacchi et al. (2018) and Dalton et al. (2020, 2024) (Fig. 10).

A. **18 ka cal BP:** The research area was completely covered under the LIS during the LGM (e.g., Fairbanks, 1989; Shaw et al., 2006; Forbes et al., 2014; Dalton et al., 2020) (Fig. 10), which resulted in the deposition of glacial till (U1) (Figs. 2 and 10; Table 1). Deglaciation in the Gulf of St. Lawrence region began ~16 ka BP and was accompanied by a rapid ice disintegration, massive calving events and a rapid post-glacial transgression (Shaw et al., 2002, 2006; Dyke et al., 2003; Shaw, 2005).

B. **LGM to ~13.6 ka cal BP**: Our data indicate marine sedimentation (U3) as early as 13.6 ± 0.12 ka BP or at the latest 12.8 ± 0.18 ka BP, which suggests that ice retreat and RSL rise occurred before this period (Fig. 10; Table 2, S2). This observation is generally consistent with previous studies that proposed a rapid rise in RSL in the region following the retreat of the LIS (e.g., Shaw et al., 2002; Dyke et al.,

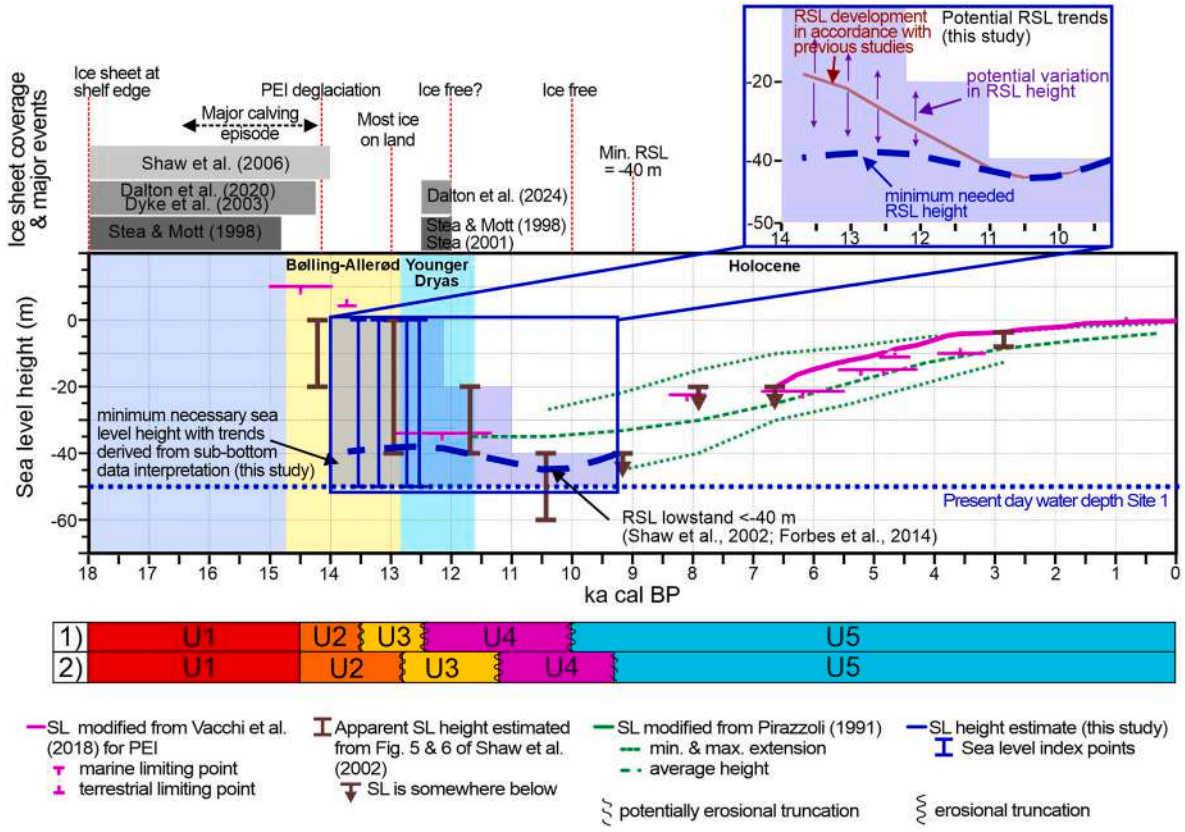

Fig. 10. Diagram showing different reconstructions for the ice history and relative sea level (RSL) development from 18 ka cal BP to present-day. Data used are modified from Pirazzoli (1991), Stea and Mott (1998), Dyke et al. (2003), Shaw et al. (2002, 2006), Stea (2011), Vacchi et al. (2018) and Dalton et al. (2020, 2024). Note that sea level predictions pre-14 ka BP are not plotted in the diagram as the region is suggested to have been covered by ice. Time is plotted as calibrated years before present. Findings from this study are shown in blue in the diagram and are highlighted in the box on the upper right corner. Our reconstruction includes an estimated minimum, pre-Holocene RSL and the likely RSL development by incorporating findings from the previous studies (red line with violet arrows). We plotted the observed sediment units below the diagram, which indicates their apparent time of deposition according to our dating and interpretation based on (1) ΔR -83 a and (2) using ΔR 600 a for sediments >10 ka (section 5.2). Note that the age of U1-U2 and U4-U5 boundaries are speculative. (For interpretation of the references to color in this figure legend, the reader is referred to the Web version of this article.)

2003; Dalton et al., 2020). Our data, however, indicate that the initial sedimentation (U2) following the ice mass retreat occurred under low energy condition, given the conformable reflection characteristic of the sediments that are present within deeper shelf sections (Table 1) (cf., Stea et al., 1996). For U2 deposition, we invoke energy damping by sea ice or possibly floating glacial ice as well as ice remnants covering the shallow basins and channels, although a lagoonal environment cannot be discounted (Fig. 9). The presence of an erosional truncation (horizon R3) on top of U2 sediments indicates a change in the depositional conditions, likely in the form of intensified wave and current activity, possibly associated with re-sedimentation (cf., Stea et al., 1996), which we associate with an absence of the previously sheltering conditions (e.g., sea ice). It is possible that U2 sediments were partially eroded in the process, which would explain the restriction of this unit to the deeper basins and channels of the shelf (Figs. 3 and 5a & b). The erosional truncation therefore represents a shift from the deposition of meltwater derived glaciomarine or -lacustrine mud (U2) to glaciomarine and marine sediments (U3) (Early Bølling-Allerød to early Younger Dryas, 14.6–12.8 ka BP). The presence of U2 and thickness of U3 suggests that the LIS itself had retreated at the latest before 13.5 ka BP, which we propose was pre-14 ka BP. This interpretation differs from the reconstruction of Stea et al. (1998), Dyke et al. (2003), Shaw et al. (2006) and Dalton et al. (2020) who indicated full ice coverage across our study site north of PEI (Site 1) at 14 ka BP (Fig. 10), as well as that the ice margin only reached the modern PEI onshore area about 13.5 ka ago (Vacchi et al., 2018).

C. **13.6 to 10 ka cal BP:** The pre- and proglacial basins and channels were filled with glaciomarine to marine sediments (U2 & U3) (Figs. 3 and 7). Foraminifera from U3 sediments north of PEI (Site 1), which can be used as index points for the water depth (cf. Vacchi et al., 2018), indicate continued deposition under shallow marine conditions (<50 mwd) between 13.6 ± 0.12 and possibly 11.3 ± 0.26 ka cal BP (Fig. 10; Table 2, S2). We therefore propose a water depth of at least 10 ± 5 m during the deposition of U3 sediments (Fig. 10). In addition, Shaw et al. (2002) suggested that to the east of PEI the post-glacial transgression resulted in RSL below the present-day sea level. The RSL was thus likely between −40 ± 5 m and <0 m (Fig. 10). Previous studies further proposed a RSL lowstand at −40 m around 10 to 9 ka cal BP, which exposed wide sections of the modern shelf to subaerial conditions (Forbes et al., 2004, 2014; Shaw, 2005; Vacchi et al., 2018) (Fig. 10). Given uncertainties in our dating, this event may be present in our data in the form of an erosional truncation (horizon R4 or potentially R5, Figs. 9 and 10).

D. **10 ka cal BP to present day:** A continuous RSL rise during the Holocene with present-day rates as high as 3.2 mm a^{-1} (Forbes et al., 2004; Shaw, 2005; Vacchi et al., 2018) brought the coast to its current position (Fig. 10). This rise in RSL was likely initiated by a combination of eustatic RSL rise and isostatic subsidence that is reported to date back to the early Holocene. (Person et al., 2003; Forbes et al., 2004, 2014). It is likely that the erosional truncation at horizon R6 and consequent change in the development of sinuous channels and the extent of sediment drifts (U5) are directly driven by a change in RSL during the early phase of the Holocene (Fig. 3, Table 1).

6. Conclusion

The landscape of the Gulf of St. Lawrence offshore PEI, as a formerly glaciated continental shelf, was notably affected by the Pleistocene glaciations. Using sub-bottom profiles and sediment cores, we reconstructed the sedimentation history since the LGM. Our study shows that the last glaciation and deglaciation period, significantly altered the morphology and influenced sedimentation in the region. Numerous buried sediment basins and channels are present down to 40 m sub-bottom depth, which were likely formed due to glacial erosion. They contain till at their base and are partially or fully filled with late Pleistocene glaciolacustrine, glaciomarine and marine sediments (13.6–11.3 ka cal BP), deposited primarily under shallow marine conditions at sedimentation rates of 0.4–1 cm a^{-1}, likely highest during the Younger Dryas. We argue that this rapid sedimentation occurred when large amounts of sediment material were redistributed offshore as a consequence of increased storm-wave and current activity and readvancing Younger Dryas ice, as the climate conditions deteriorated. We further observe an erosional truncation of the sediment package deposited during the mid-Younger Dryas to early Holocene transition. Given uncertainties in dating of older sediment material this truncation is either possibly related to: 1) increased storm-wave activity in combination with a reduction in RSL due to isostatic uplift or ice built-up during the Younger Dryas; or 2) an RSL lowstand, as proposed by others for the late Pleistocene to early Holocene transition. This erosional truncation is overlain by an up to 4 m thick sediment package of chaotic characteristic, which was deposited between the mid-Younger Dryas and early Holocene. Given its timing and thickness distribution, we suggest that this sediment package either resulted from meltwater deposition or deposition during the RSL lowstand. Its chaotic appearance with remnants of interbedded parallel reflections indicates sediment disturbance possibly due to storm waves or sea ice grounding. These layers are overlain by Holocene sediments that are locally up to 7 m thick, indicating a change from more turbulent to calm sedimentation conditions.

This study provides one of the few examples of dated Younger Dryas sediments in Atlantic Canada. The findings show that the Bølling-Allerød and especially the Younger Dryas event had a large influence on sedimentation within the research area, as a significant portion of sediment was deposited during the relatively short duration of this event (1300 a). Our data further show an erosional truncation that is possibly related to the Holocene RSL lowstand as depicted in previous models but could also be related to a change in RSL development and increased storm-wave activity during the Younger Dryas.

Author contribution

I.S. conceptualized the study and wrote the first draft with V.M. I.S. did the data analysis and interpretations with contributions from V.M., E.L.K., C.B., A.M., C.J.B., J.E., B.K. and M.N. M.S., T.M., and C.H. performed the geochemical data analysis. A.A. performed the foraminiferal analysis and provided information about the biofacies. S.H., F.C.R. and I. S. were involved with the initial data collection and S.H., F.C.R., A.K. and S.Y. provided feedback on the manuscript. V.M. and M.N. supervised the overall project and provided funding. All authors have discussed the results and helped drafting the final manuscript.

Declaration of competing interest

The authors declare that they have no known competing financial interests or personal relationships that could have appeared to influence the work reported in this paper.

Acknowledgements

This study has been supported by the SOURCE Project funded by the Ocean Frontier Institute (Canada). We are grateful to the crew of the research expedition MSM103.The software ps32sgy developed by Hanno Keil (University of Bremen) was used to convert Parasound data into SEG-Y formats usable in Kingdom Suite™. We appreciate helpful comments from the editor and the three anonymous reviewers.

Appendix A. Supplementary data

Supplementary data to this article can be found online at https://doi.org/10.1016/j.quascirev.2025.109715.

Data availability

All data and/or code is contained within the submission.

References

Alve, E., Korsun, S., Schönfeld, J., Dijkstra, N., Golikova, E., Hess, S., Husum, K., Panieri, G., 2016. Foram-AMBI: a sensitivity index based on benthic foraminiferal faunas from North-East Atlantic and Arctic fjords, continental shelves and slopes. Mar. Micropaleontol. 122, 1–12.

Barlow, P.M., Reichard, E.G., 2010. Saltwater intrusion in coastal regions of North America. Hydrogeol. J. 18 (1), 247.

Barrie, C.Q., Piper, D.J., 1982. Late Quaternary Marine Geology of Makkovik Bay, Labrador, vol. 17. Geological Survey of Canada, pp. 1–41.

Batchelor, C.L., Dowdeswell, J.A., Hogan, K.A., 2011. Late Quaternary ice flow and sediment delivery through Hinlopen Trough, Northern Svalbard margin: submarine landforms and depositional fan. Mar. Geol. 284 (1–4), 13–27.

Bernhard, J.M., Bowser, S.S., 1999. Benthic Foraminifera of dysoxic sediments: chloroplast sequestration and functional morphology. Earth Sci. Rev. 46, 149–165.

Borns Jr., H.W., Doner, L.A., Dorion, C.C., Jacobson Jr., G.L., Kaplan, M.R., Kreutz, K.J., Lowell, T.V., Thompson, W.B., Weddle, T.K., 2004. The deglaciation of Maine, U.S.A. In: Ehlers, J., Gibbard, P.L. (Eds.), Quaternary Glaciations—Extent and Chronology, Part II. North America. Elsevier, Amsterdam, pp. 89–109.

Brady, H.B., 1884. Report on the Foraminifera dredged by HMS Challenger, during the years 1873-1876: report on the scientific results of the Voyage of HMS Challenger. Zoology 9, 1–814.

Brauer, A., Haug, G.H., Dulski, P., Sigman, D.M., Negendank, J.F., 2008. An abrupt wind shift in western Europe at the onset of the Younger Dryas cold period. Nat. Geosci. 1 (8), 520–523.

Cage, A.G., Pieńkowski, A.J., Jennings, A., Knudsen, K.L., Seidenkrantz, M.S., 2021. Comparative analysis of six common foraminiferal species of the genera Cassidulina, Paracassidulina, and Islandiella from the Arctic-North Atlantic domain. J. Micropalaeontol. 40, 37–60.

Carr, P.A., 1969. Salt-water intrusion in Prince Edward Island. Can. J. Earth Sci. 6 (1), 63–74.

Clark, P.U., Dyke, A.S., Shakun, J.D., Carlson, A.E., Clark, J., Wohlfarth, B., Mitrovica, J. X., Hostetler, S.W., McCabe, A.M., 2009. The last glacial maximum. science 325 (5941), 710–714.

Cook, S.J., Swift, D.A., 2012. Subglacial basins: their origin and importance in glacial systems and landscapes. Earth Sci. Rev. 115 (4), 332–372.

Correggiari, A., Cattaneo, A., Trincardi, F., 2005. The modern Po Delta system: lobe switching and asymmetric prodelta growth. Mar. Geol. 222, 49–74.

Dalton, A.S., Margold, M., Stokes, C.R., Tarasov, L., Dyke, A.S., Adams, R.S., Allard, S., Arends, H.E., Atkinson, N., Attig, J.W., Barnett, P.J., 2020. An updated radiocarbon-based ice margin chronology for the last deglaciation of the North American Ice Sheet Complex. Quat. Sci. Rev. 234, 106223.

Dalton, A.S., Margold, M., Dulfer, H.E., Norris, S.L., Tarasov, L., 2024. Response of North American ice sheets to the Younger Dryas cold reversal (12.9 to 11.7 ka). Earth Sci. Rev. 255, 104845.

Dhavamani, R., Pipík, R., Sočuvka, V., Šurka, J., Starek, D., Milovský, R., Uhlík, P., Vidhya, M., Žatková, L., Král', P., 2022. Sub-bottom and bathymetry sonar inspection of postglacial lacustrine infill of the alpine lakes (Tatra Mts., Slovakia). Catena 209, 105787.

Dowdeswell, J.A., Fugelli, E.M.G., 2012. The seismic architecture and geometry of grounding-zone wedges formed at the marine margins of past ice sheets. Bulletin 124 (11–12), 1750–1761.

Dubey, K.M., Chaubey, A.K., Mahale, V.P., Karisiddaiah, S.M., 2019. Buried channels provide keys to infer Quaternary stratigraphic and paleo-environmental changes: a case study from the west coast of India. Geosci. Front. 10 (4), 1577–1595.

Dyke, A.S., Moore, A., Robertson, L., 2003. Deglaciation of North America. Geological Survey of Canada. https://doi.org/10.4095/214399. Open File 1574.

Edmunds, W.M., Hinsby, K., Marlin, C., Condesso de Melo, M.T., Manzano, M., Vaikmae, R., Travi, Y., 2001. Evolution of groundwater systems at the European coastline. Geological Society, London, Special Publications 189 (1), 289–311.

Evans, D.J., Evans, I.S., 2022. Glacial processes and landforms. Geol. Soc. Lond. Mem. 58, 333–377. https://doi.org/10.1144/M58-2021-17.

Fairbanks, R.G., 1989. A 17,000-year glacio-eustatic sea level record: influence of glacial melting rates on the Younger Dryas event and deep-ocean circulation. Nature 342 (6250), 637–642.

Forbes, D.L., Parkes, G.S., Manson, G.K., Ketch, L.A., 2004. Storms and shoreline retreat in the southern Gulf of st. Lawrence. Mar. Geol. 210 (1–4), 169–204.

Forbes, D.L., Manson, G.K., Whalen, D.J.R., Couture, N.J., Hill, P.R., 2014. Coastal products of marine transgression in cold-temperate and high-latitude coastal-plain settings: gulf of St Lawrence and Beaufort Sea. Geological Society, London, Special Publications 388 (1), 131–163.

Fulthorpe, C.S., Austin Jr, J.A., 2004. Shallowly buried, enigmatic seismic stratigraphy on the New Jersey outer shelf: evidence for latest Pleistocene catastrophic erosion? Geology 32 (12), 1013–1016.

García-García, A., García-Gil, S., Vilas, F., 2004. Echo characters and recent sedimentary processes as indicated by high-resolution sub-bottom profiling in Ría de Vigo (NW Spain). Geo Mar. Lett. 24, 32–45.

Gibling, M.R., Culshaw, N., Pascucci, V., Waldron, J.W.F., Rygel, M.C., 2019. The Maritimes Basin of Atlantic Canada: Basin creation and destruction during the Paleozoic assembly of pangea. In: The Sedimentary Basins of the United States and Canada. Elsevier, pp. 267–314.

Goosse, H., Roche, D.M., Mairesse, A., Berger, M., 2013. Modelling past sea ice changes. Quat. Sci. Rev. 79, 191–206.

Hald, M., Korsun, S., 1997. Distribution of modern benthic Foraminifera from fjords of Svalbard, European Arctic. J. Foraminifer. Res. 27, 101–122.

Hansen, H.J., Lykke-Andersen, A.L., 1976. Wall structure and classification of fossil and recent elphidiid and nonionid Foraminifera. Foss. Strata 10, 1–37.

Hayward, B.W., Le Coze, F., Vachard, D., Gross, O., 2025. World Foraminifera database. https://www.marinespecies.org/foraminiferaon2025-02-09.

Heaton, T.J., Köhler, P., Butzin, M., Bard, E., Reimer, R.W., Austin, W.E., Ramsey, C.B., Grootes, P.M., Hughen, K.A., Kromer, B., Reimer, P.J., 2020. Marine20—the marine radiocarbon age calibration curve (0–55,000 cal BP). Radiocarbon 62 (4), 779–820.

Hodell, D.A., Evans, H.F., Channell, J.E., Curtis, J.H., 2010. Phase relationships of North Atlantic ice-rafted debris and surface-deep climate proxies during the last glacial period. Quat. Sci. Rev. 29 (27–28), 3875–3886.

Hogan, K.A., Jakobsson, M., Mayer, L., Reilly, B.T., Jennings, A.E., Stoner, J.S., Nielsen, T., Andresen, K.J., Nørmark, E., Heirman, K.A., Kamla, E., 2020. Glacial sedimentation, fluxes and erosion rates associated with ice retreat in Petermann Fjord and Nares Strait, north-west Greenland. Cryosphere 14 (1), 261–286.

Hölz, S., 2022. Groundwater resources offshore Prince Edward Island, Canada cruise No. MSM103, 12.9.–15.11. 2021. Emden (Germany)–Halifax (Canada)–Emden (Germany). PRINCE.

IPCC, 2023. In: Sections 2 and 3. In: Climate Change 2023: Synthesis Report. Contribution of Working Groups I, II and III to the Sixth Assessment Report of the Intergovernmental Panel on Climate Change [Core Writing Team. IPCC, Geneva, Switzerland, pp. 35–115. https://doi.org/10.59327/IPCC/AR6-9789291691647.

Janocko, M., Nemec, W., Henriksen, S., Warchoł, M., 2013. The diversity of deep-water sinuous channel belts and slope valley-fill complexes. Mar. Petrol. Geol. 41, 7–34.

Jennings, A.E., Helgadottir, G., 1994. Foraminiferal assemblages from the fjords and shelf of eastern Greenland. J. Foraminifer. Res. 24, 123–144.

Jiang, Y., Somers, G., 2009. Modeling effects of nitrate from non-point sources on groundwater quality in an agricultural watershed in Prince Edward Island, Canada. Hydrogeol. J. 17 (3), 707.

Josenhans, H.W., Fader, G.B.J., 1989. A comparison of models of glacial sedimentation along the eastern Canadian margin. Mar. Geol. 85 (2–4), 273–300.

Josenhans, H., Lehman, S., 1999. Late glacial stratigraphy and history of the Gulf of st. Lawrence, Canada. Can. J. Earth Sci. 36 (8), 1327–1345.

Josenhans, H.W., Zevenhuizen, J., Klassen, R.A., 1986. The Quaternary geology of the Labrador shelf. Can. J. Earth Sci. 23 (8), 1190–1213.

Josenhans, H., Zevenhuizen, J., MacLean, B., 1990. Preliminary Seismostratigraphic Interpretations from the Gulf of St. Lawrence. Geological Survey of Canada, Current Research, Part B, pp. 59–75. Paper.

Kleiber, H.P., Niessen, F., Weiel, D., 2001. The Late Quaternary evolution of the western Laptev Sea continental margin, Arctic Siberia—Implications from sub-bottom profiling. Global Planet. Change 31 (1–4), 105–124.

Klotsko, S., Driscoll, N., Keigwin, L., 2019. Multiple meltwater discharge and ice rafting events recorded in the deglacial sediments along the Beaufort Margin, Arctic Ocean. Quat. Sci. Rev. 203, 185–208.

Kongsberg, 2022. EM712 – multibeam Echo sounder, datasheet. https://www.kongsberg.com/discovery/seafloor-mapping/em/em712/. Open Document, Norway.

Lohrberg, A., Schmale, O., Ostrovsky, I., Niemann, H., Held, P., Schneider von Deimling, J., 2020. Discovery and quantification of a widespread methane ebullition event in a coastal inlet (Baltic Sea) using a novel sonar strategy. Sci. Rep. 10 (1), 4393.

Loring, D.H., Nota, D.J.G., 1973. Morphology and sediments of the Gulf of st. Lawrence. Fisheries Research Board of Canada. Bulletin 182, 1–147.

Lundmark, K., 2017. Acoustic Survey of Sea Floor Features in Asköfjärden. Stockholm University, Stockholm, Sweden, p. 51. BSc. thesis, urn:nbn:se:su:diva-143790.

Maselli, V., Hutton, E.W., Kettner, A.J., Syvitski, J.P., Trincardi, F., 2011. High-frequency sea level and sediment supply fluctuations during Termination I: an integrated sequence-stratigraphy and modeling approach from the Adriatic Sea (Central Mediterranean). Mar. Geol. 287 (1–4), 54–70.

McNeely, R., Dyke, A.S., Southon, J.R., 2006. Canadian Marine Reservoir Ages, Preliminary Data Assessment, Open File 5049. Geological Survey Canada, p. 3.

Melles, M., Kuhn, G., 1993. Sub-bottom profiling and sedimentological studies in the southern Weddell Sea, Antarctica: evidence for large-scale erosional/depositional processes. Deep Sea Res. Oceanogr. Res. Pap. 40 (4), 739–760.

Micallef, A., Averes, T., Hoffmann, J., Crutchley, G., Mountjoy, J.J., Person, M., Cohen, D., Woelz, S., Bury, S.J., Ahaneku, C.V., Spatola, D., 2022. Multiple drivers and controls of pockmark formation across the Canterbury Margin, New Zealand. Basin Res. 34 (4), 1374–1399.

Mitchum Jr., R.M., Vail, P.R., Thompson S., I.I.I., 1977. Seismic stratigraphy and global changes of sea level: part 2. The depositional sequence as a basic unit for stratigraphic analysis: section 2. Application of Seismic Reflection Configuration to Stratigraphic Interpretation.

Papatheodorou, G., Geraga, M., Christodoulou, D., Fakiris, E., Iatrou, M., Georgiou, N., Dimas, X., Ferentinos, G., 2021. The Battle of Lepanto search and survey mission (1971–1972) by Throckmorton, Edgerton and Yalouris: following their traces half a century later using marine geophysics. Remote Sens. 13 (16), 3292.

Patton, H., Swift, D.A., Clark, C.D., Livingstone, S.J., Cook, S.J., 2016. Distribution and characteristics of overdeepenings beneath the Greenland and Antarctic ice sheets: implications for overdeepening origin and evolution. Quat. Sci. Rev. 148, 128–145.

Person, M., Dugan, B., Swenson, J.B., Urbano, L., Stott, C., Taylor, J., Willett, M., 2003. Pleistocene hydrogeology of the Atlantic continental shelf, New England. Geol. Soc. Am. Bull. 115 (11), 1324–1343.

Pinet, N., Brake, V., 2024. Aeromagnetic data reveals buried Quaternary drainage patterns in the Gulf of St Lawrence (Canada). J. Geol. Soc. 181 (6), 2024–2057.
Piper, D.J.W., Fehr, S.D., 1991. Radiocarbon chronology of late Quaternary sections on the inner and middle Scotian Shelf, south of Nova Scotia. In: Current Research, Part E. Geological Survey of Canada, pp. 321–325. Paper 91-1E.
Pirazzoli, P.A., 1991. World Atlas of Holocene Sea-Level Changes. Elsevier, Amsterdam, p. 117. Singapore Tide Gauge (Horsburgh Lighthouse).
Racine, C., Bonnin, J., Dessandier, P.-A., Giraudeau, J., 2023. Distribution of living benthic Foraminifera in the Baffin Bay and Nares Strait in the summer and fall periods: relation with environmental parameters. J. Mar. Sci. Eng. 11, 2049. https://doi.org/10.3390/jmse11112049.
Ramsey, C.B., 2009. Bayesian analysis of radiocarbon dates. Radiocarbon 51 (1), 337–360.
Rebesco, M., Özmaral, A., Urgeles, R., Accettella, D., Lucchi, R.G., Rüther, D., Winsborrow, M., Llopart, J., Caburlotto, A., Lantzsch, H., Hanebuth, T.J., 2016. Evolution of a high-latitude sediment drift inside a glacially-carved trough based on high-resolution seismic stratigraphy (Kveithola, NW Barents Sea). Quat. Sci. Rev. 147, 178–193.
Reimer, P.J., Austin, W.E., Bard, E., Bayliss, A., Blackwell, P.G., Ramsey, C.B., Butzin, M., Cheng, H., Edwards, R.L., Friedrich, M., Grootes, P.M., 2020. The IntCal20 Northern Hemisphere radiocarbon age calibration curve (0–55 cal kBP). Radiocarbon 62 (4), 725–757.
Rodrigues, C.G., Hooper, K., 1982. Recent benthonic foraminiferal associations from offshore environments in the Gulf of st. Lawrence. J. Foraminifer. Res. 12 (4), 321–352.
Rytter, F., Knudsen, K.L., Seidenkrantz, M.S., Eiríksson, J., 2002. Modern distribution of benthic Foraminifera on the North Icelandic shelf and slope. J. Foraminifer. Res. 32, 217–244.
Schafer, C.T., Cole, F.E., 1982. Living benthic Foraminifera distributions on the continental slope and rise east of Newfoundland, Canada. Geological Survey of America, Bulletin 93, 207–217.
Schmidt, C., Geslin, E., Bernhard, J.M., LeKieffre, C., Svenning, M.M., Roberge, H., Schweizer, M., Panieri, G., 2022. Deposit-feeding of Nonionellina labradorica (foraminifera) from an Arctic methane seep site and possible association with a methanotroph. Biogeosciences 19, 3897–3909.
Schröder-Adams, C.J., Cole, F.E., Medioli, F.S., Mudie, P.J., Scott, D.B., Dobbin, L., 1990. Recent Arctic shelf foraminifera: seasonally ice covered vs. perennial ice-covered areas. J. Foraminifer. Res. 20, 8–36.
Scott, D.B., Vilks, G., 1991. Benthonic Foraminifera in the surface sediments of the deep-sea Arctic Ocean. J. Foraminifer. Res. 21, 20–38.
Scott, D.B., Medioli, F.S., Schafer, C.T., 1977. Temporal changes in Foraminifera distributions in Miramichi River estuary New Brunswick. Can. J. Earth Sci. 14 (7), 1566–1587.
Scott, D.B., Schafer, C.T., Medioli, F.S., 1980. Eastern Canadian estuarine foraminifera: a framework for comparison. Journal of Foramiferal Research 10 (3), 205–234.
Scott, D.B., Medioli, F.S., Schafer, C.T., 2001. Monitoring in Coastal Environments Using Foraminifera and Thecamoebian Indicators. Cambridge University Press, Cambridge, p. 177.
Shaw, J., 2005. Geomorphic evidence of postglacial terrestrial environments on Atlantic Canadian continental shelves. Géogr. Phys. Quaternaire 59 (2), 141–154.
Shaw, J., Gareau, P., Courtney, R.C., 2002. Palaeogeography of Atlantic Canada 13–0 kyr. Quat. Sci. Rev. 21 (16–17), 1861–1878.
Shaw, J., Piper, D.J.W., Fader, G.B.J., King, E.L., Todd, B.J., Bell, T., Batterson, M.J., Liverman, D.G.E., 2006. A conceptual model of the deglaciation of Atlantic Canada. Quat. Sci. Rev. 25 (17–18), 2059–2081.
Shaw, J., Todd, B.J., Brushett, D., Parrott, D.R., Bell, T., 2009. Late Wisconsinan glacial landsystems on Atlantic Canadian shelves: new evidence from multibeam and single-beam sonar data. Boreas 38 (1), 146–159.
Słowiński, M., Zawiska, I., Ott, F., Noryśkiewicz, A.M., Plessen, B., Apolinarska, K., Rzodkiewicz, M., Michczyńska, D.J., Wulf, S., Skubała, P., Kordowski, J., 2017. Differential proxy responses to late Allerød and early Younger Dryas climatic change recorded in varved sediments of the Trzechowskie palaeolake in Northern Poland. Quat. Sci. Rev. 158, 94–106.
Spieß, V., 1993. Digitale Sedimentechographie – neue Wege zu einer hochauflösenden Akustostratigraphie. Berichte Fachbereich Geowissenschaften Univ. Bremen 35, 1–199.
Stanic, S., LeRoux, N.K., Paldor, A., Mohammed, A.A., Michael, H.A., Kurylyk, B.L., 2024. Saltwater intrusion into a confined island aquifer driven by erosion, changing recharge, sea-level rise, and coastal flooding. Water Resour. Res. 60 (1), e2023036394.
Stea, R.R., 2011. Appalachian Glacier complex in Maritime Canada. In: Singh, V.P., Singh, P., Haritashya, U.K. (Eds.), Encyclopedia of Snow, Ice and Glaciers. Encyclopedia of Earth Sciences Series. Springer, Dordrecht. https://doi.org/10.1007/978-90-481-2642-2_25.
Stea, R.R., Mott, R.J., 1989. Deglaciation environments and evidence for glaciers of Younger Dryas age in Nova Scotia, Canada. Boreas 18 (2), 169–187.
Stea, R.R., Mott, R.J., 1998. Deglaciation of Nova Scotia: stratigraphy and chronology of lake sediment cores and buried organic sections. Géogr. Phys. Quaternaire 52 (1), 3–21.
Stea, R.R., Mott, R.J., 2005. Younger Dryas glacial advance in the southern Gulf of st. Lawrence, Canada: analogue for ice inception? Boreas 34 (3), 345–362.
Stea, R.R., Boyd, R., Costello, O., Fader, G.B.J., Scott, D.B., 1996. Deglaciation of the inner Scotian Shelf. Nova Scotia: correlation of terrestrial and marine glacial events. Geological Society, London, Special Publications 111 (1), 77–101.
Stea, R.R., Piper, D.J.W., Fader, G.B.J., Boyd, R., 1998. Wisconsinan glacial and sea-level history of Maritime Canada and the adjacent continental shelf: a correlation of land and sea events. Geol. Soc. Am. Bull. 110 (7), 821–845.
Stokes, C.R., 2017. Deglaciation of the Laurentide ice sheet from the last glacial maximum. Cuadernos de investigación geográfica 43 (2).
Symons, D.T.A., 1990. Early Permian pole: evidence from the Pictou red beds, Prince Edward Island, Canada. Geology 18 (3), 234–237.
Teledyne Marine, 2017. ATLAS PARASOUND deep-sea parametric sub-bottom profiler. http://www.teledynemarine.com/parasound-sub-bottom-profilers?ProductLineID=79/.Slangerup,Denmark. (Accessed 21 October 2022).
Thomas, F.C., Medioli, F.S., Scott, D.B., 1990. Holocene and latest Wisconsinan benthic foraminiferal assemblages and paleocirculation history, lower Scotian slope and rise. J. Foraminifer. Res. 20 (3), 212–245.
Thompson, W.B., Griggs, C.B., Miller, N.G., Nelson, R.E., Weddle, T.K., Kilian, T.M., 2011. Associated terrestrial and marine fossils in the late-glacial Presumpscot Formation, southern Maine, USA, and the marine reservoir effect on radiocarbon ages. Quaternary Research 75 (3), 552–565.
Todd, R., Low, D., 1981. Marine Flora and Fauna of the Northeastern United States. Protozoa: Sarcodina: benthic Foraminifera. Series: NOAA Technical Report NMFS CIRC; 439. National Marine Fisheries Service, United States. https://repository.library.noaa.gov/view/noaa/5425.
Toomey, M.R., Korty, R.L., Donnelly, J.P., van Hengstum, P.J., Curry, W.B., 2017. Increased hurricane frequency near Florida during Younger Dryas Atlantic meridional overturning circulation slowdown. Geology 45 (11), 1047–1050.
Tremblay, T., Lamothe, M., 2007. In: Late Quaternary geomorphology and geochronology near Covey Hill, and an ice stream deglaciation model for the southern St-Lawrence Valley, Vol. 39. In: Geological Society of America Abstracts with Programs, p. 56. No. 1.
Trincardi, F., Cattaneo, A., Correggiari, A., Ridente, D., 2004. Evidence of soft sediment deformation, fluid escape, sediment failure and regional weak layers within the late Quaternary mud deposits of the Adriatic Sea. Mar. Geol. 213 (1–4), 91–119.
Vacchi, M., Engelhart, S.E., Nikitina, D., Ashe, E.L., Peltier, W.R., Roy, K., Kopp, R.E., Horton, B.P., 2018. Postglacial relative sea-level histories along the eastern Canadian coastline. Quat. Sci. Rev. 201, 124–146.
Van de Poll, H.W., 1989. Lithostratigraphy of the Prince Edward Island redbeds. Atl. Geol. 25 (1), 23–35.
Vilks, G., 1969. Recent Foraminifera in the Canadian arctic. Micropaleontology 15 (1), 35–60.
Vilks, G., 1989. Ecology of recent Foraminifera on the Canadian Continental Shelf of the Arctic Ocean. In: Herman, Y. (Ed.), The Arctic Seas: Climatology, Oceanography, Geology, and Biology. Van Nostrand Reinhold, New York, pp. 497–569.
Vilks, G., Deonarine, B., Wagner, F.J., Winters, G.V., 1982. Foraminifera and Mollusca in surface sediments of southeastern Labrador Shelf. Geol. Soc. Am. Bull. 93, 225–238.
Williamson, M.A., Keen, C.E., Mudie, P.J., 1984. Foraminiferal distribution on the continental margin off Nova Scotia. Mar. Micropaleontol. 9 (3), 219–239.
Winsborrow, M.C., Andreassen, K., Corner, G.D., Laberg, J.S., 2010. Deglaciation of a marine-based ice sheet: late Weichselian palaeo-ice dynamics and retreat in the southern Barents Sea reconstructed from onshore and offshore glacial geomorphology. Quat. Sci. Rev. 29 (3–4), 424–442.
Yu, S., Kurylyk, B.L., Michael, H.A., Maselli, V., Nedimović, M.R., Schulten, I., Córdoba-Ramírez, F., 2025. Numerical investigation of offshore freshened groundwater dynamics in a changing marine environment. J. Hydrol., 134553
Zecchin, M., Rebesco, M., 2018. Glacigenic and glacimarine sedimentation from shelf to trough settings in the NW Barents Sea. Mar. Geol. 402, 184–193.
Zecchin, M., Rebesco, M., Lucchi, R.G., Caffau, M., Lantzsch, H., Hanebuth, T.J., 2016. Buried iceberg-keel scouring on the southern Spitsbergenbanken, NW Barents Sea. Mar. Geol. 382, 68–79.